EARLY ONLINE RELEASE

This is a preliminary PDF of the author-produced manuscript that has been peer-reviewed and accepted for publication. Since it is being posted so soon after acceptance, it has not yet been copyedited, formatted, or processed by AMS Publications. This preliminary version of the manuscript may be downloaded, distributed, and cited, but please be aware that there will be visual differences and possibly some content differences between this version and the final published version.

Dynamical Downscaling of the Climate for the Hawaiian Islands

Part I: Present-day

Chunxi Zhang, Yuqing Wang[1], Kevin Hamilton, Axel Lauer[2]

International Pacific Research Center and Department of Atmospheric Sciences, School of

Ocean and Earth Science and Technology, University of Hawaii at Manoa, Honolulu, HI

June 22, 2015 (submitted)

February 1, 2016 (revised)

Dateline

_____

[1]Corresponding author: Dr. Yuqing Wang, International Pacific Research Center, SOEST, University of Hawaii at Manoa, 1680 East-West Road, Honolulu, HI 96822, E-mail: yuqing@hawaii.edu

[2]Current affiliation: DLR Institute of Atmospheric Physics, Oberpfaffenhofen, Germany

Abstract

Hawaii's high and steep topography leads to pronounced small scale variations in climate and this makes comprehensive modeling of the weather and climate particularly challenging. This paper describes a regional model formulation designed for simulations of the microclimates in Hawaii, and then documents and analyzes an extended retrospective simulation for near present day conditions. Part II will apply the model to projected climate conditions near the end of the present century.

A nested version of the advanced Weather Research and Forecasting model with fine horizontal resolution and improved physics for the Hawaiian region has been configured. A 20-year triply-nested simulation of the atmospheric flow was undertaken with a 3-km resolution mesh covering all main Hawaiian Islands and a 1-km mesh over Maui. Ocean surface temperatures are prescribed from observations and meteorological fields at the boundaries of the outermost domain are taken from global reanalyses. The simulations are compared to surface, balloon and satellite observations over the same period. The 3-km version of the model simulates realistically the frequency of trade wind inversions, time-mean rainfall and other variables on relatively small scales over Hawaii Island. There is a reasonable agreement between observed and simulated mean rainfall patterns over the other islands as well. However, the simulated distribution of mean rainfall over Kauai and (most particularly) Maui and Oahu reveals some significant deficiencies which we attribute to inadequate resolution of the topography on these islands. The 1-km simulation over Maui shows clear improvement in the mean rainfall over the 3-km version.

1. Introduction

The application of limited area dynamical atmospheric models to simulate fields at fine horizontal scales that are consistent with coarser scale global analyses or global general circulation model (GCM) simulations is being actively pursued for many geographical areas around the world (e.g., Laprise et al. 1998; Wang et al. 2004; Fu et al. 2005; Rummukainen 2010; Mearns et al. 2012; Rasmussen et al. 2014; Mahoney et al. 2013). Much of the current interest is motivated by the desire to provide local-scale climate change projections consistent with global coupled ocean-atmosphere model results (e.g., Mearns et al. 2012). This "dynamical downscaling" via regional comprehensive models is also potentially useful for seasonal climate prediction. In addition, retrospective simulations with limited area models forced by observed boundary conditions could find application in understanding and modeling the fine scale dependence of aspects of the local environment such as ground water availability, nutrient deposition to the soil, the ecology of plant communities, etc.

Regularly gridded global reanalyses of the observed atmospheric fields are now produced by several major meteorological centers throughout the world, and generally such gridded fields are made available at ~50-300 km horizontal spacing. The ~50-300 km grid spacing is also typical of the global coupled models now being run for long term climate projections (e.g., Taylor et al. 2012). For many locations and particular applications, there is some interest in dynamically downscaled fields at even only moderately finer resolution. For example, the US multiagency "North American Regional Climate Change Assessment Program" (NARCCAP) involves downscaling a large number of coupled global model projections for the North American region using several regional atmospheric models run at about 50 km horizontal resolution (Mearns et al. 2012). A somewhat similar program (referred to as USGS RegCLIM)

led by the US Geological Survey is producing downscaled climate projections for large parts of North America using a regional model with ~15 km horizontal resolution (Hostetler et al. 2011). While such dynamical downscaling datasets may be valuable for many regions, they would have very little applicability to the Hawaiian Islands where the unusual geography results in very fine scale microclimatic gradients.

State-of-the-art global models with a horizontal resolution of ~100 km or coarser may represent all the Hawaiian Islands as just a handful of land grid-boxes. Without an adequate representation of the very high and steep topographic relief characteristic of Hawaii, such models cannot simulate even basic features of the winds, temperature and rainfall over the Hawaiian Islands. Notably, even a first-order representation of the observed intra-island geographical distribution of rainfall clearly requires using a model with much finer resolution than those now employed in the NARCCAP or USGS RegCLIM downscaling exercises.

In their recent review, Harter et al. (2015) provide an overview on the impacts of global climate change on the flora of oceanic islands. Even though the authors emphasize the importance and the need for more and better climate data and models on the island scale, only very few studies applying very high resolution dynamical downscaling for the oceanic islands exist at present. Examples of such studies include, for instance, Morel et al. (2014) who documented the capabilities of the advanced Weather Research and Forecasting model (WRF, e.g., Skamarock et al. 2008) to simulate rainfall at very fine (680 m) spatial resolution over La Réunion. Similar to Hawaii, La Réunion is a small volcanic island with complex topography and a tropical maritime climate with two marked seasons. Pérez et al. (2014) evaluated the WRF parameterizations for dynamical downscaling in the Canary Islands with a horizontal resolution of up to 5 km. This study showed that specific model configurations were able to reproduce

83   observations of important variables in this archipelago reasonably well, demonstrating the

84   potential for regional climate change simulations. Kendon et al. (2014) used a multiply-nested

85   regional atmospheric model to downscale a global GCM climate simulation for a region in

86   southern England and employed an inner grid with 1.5-km resolution. The application of very

87   high resolution regional models has been reviewed recently by Prein et al. (2015).

88   Zhang et al. (2012a; hereafter ZWLH) configured a nested version of the WRF model with

89   both fine resolution (3 km) and improved physics appropriate for the Hawaiian region. We

90   follow ZWLH and refer to this as the Hawaiian Regional Climate Model (HRCM). Configuring

91   the HRCM involved several modifications of the publically available WRF versions. Notably

92   the HRCM includes a version of the Tiedtke convection parameterization scheme implemented

93   as described by Zhang et al. (2011), which has been made publicly available and is now part of

94   the standard WRF since version 3.3. The HRCM was then further improved by including a

95   modified cloud microphysics package and introducing a detailed specification of surface

96   properties (albedo, land cover type, soil type, and green vegetation fraction) for the Hawaiian

97   Islands (ZWLH). ZWLH discussed a one-year retrospective simulation (November 2005 to

98   October 2006) in a doubly nested version at horizontal resolutions of 15 km and 3 km over the

99   main Hawaiian Islands and the surrounding ocean region. This retrospective integration was

100   driven with observed daily sea surface temperature (SST) and horizontal boundary fields taken

101   from global meteorological reanalyses. Since then we have completed a 20-year retrospective

102   simulation (1990–2009) and a 20-year simulation driven with projected future conditions

103   representing the end of the current century (2080–2099). These new model integrations

104   employed a triply-nested version of HRCM that included a 1-km grid mesh over the island of

105   Maui and adjacent ocean regions.

106   The present paper is Part I of a two part series and reports on the 20-year retrospective

107   simulation, while Part II will discuss the projected late 21st century climate change simulation.

108   Part II will also discuss some of the specific motivations for producing fine resolution climate

109   projections for Hawaii. Note that the Pacific islands chapter of the U.S. National Climate

110   Assessment provides an up to date review of many aspects of climate change impacts seen and

111   anticipated in Hawaii (Leong et al. 2014).

112   This first paper will demonstrate that the HRCM performs well enough in simulating

113   present day microclimatic conditions that it can be applied reasonably in projecting the fine

114   structure of climate changes on individual islands. An important aim of the present paper is to

115   improve our knowledge of the advantages and limitations of high-resolution dynamical

116   downscaling with a regional climate model applied to the Hawaiian Islands. Specifically, we (i)

117   investigate the effect of improving the 3 km horizontal resolution employed by ZWLH and

118   exploring the behavior of an atmospheric model in extended simulations at 1 km resolution; (ii)

119   provide a 20-year simulation that allows more reliable statistics to be computed for comparisons

120   with observations of various kinds, notably for rainfall, including its diurnal variation; (iii)

121   evaluate how well the interannual variations in rainfall and other quantities over individual

122   locations can be captured by a high resolution model forced by observed SSTs and large-scale

123   boundary fields; and (iv) provide a first comparison of the regional geographical modulation of

124   the boundary layer structure simulated in a high-resolution model with that derived recently

125   from satellite radio occultation data (Zhang et al. 2012b).

126   The paper is organized as follows. Section 2 briefly outlines some dominant features of the

127   present day atmospheric circulation and climate for Hawaii. Section 3 describes the

128   observational datasets that we have used for evaluating the model results and briefly

129 summarizes the basic HRCM description from ZWLH and lays out the details of the

130 configuration adopted for the present simulation. Sections 4 and 5 describe aspects of the

131 simulation in the HRCM outermost and intermediate domains, respectively. Section 6 examines

132 the simulation over Maui in the 1-km resolution innermost domain. Results are discussed and

133 conclusions are summarized in Section 7.

134 **2. Meteorological background**

135 The atmospheric general circulation sets the stage for any study of Hawaii climate. Much

136 of the subtropics and adjacent tropical regions are dominated by mean sinking motion through

137 the troposphere. Over the continents this leads to the familiar subtropical deserts, while over

138 much of the tropical and subtropical oceans the large scale circulation establishes a regime

139 typified by a well-mixed marine boundary layer (MBL) capped by a temperature inversion layer.

140 Around Hawaii over 80% of atmospheric soundings can be characterized as having well defined

141 trade wind inversions (TWIs) which cap the MBL at heights ranging from 1000 to 4000 m

142 above sea level (Cao et al. 2007). Typically the TWI layer is about 300 m thick and the relative

143 humidity drops by ~40% across this layer (Cao et al. 2007). The prevailing surface winds in

144 Hawaii are from the east-northeast and, generally speaking, days with a well-defined TWI also

145 tend to have surface winds with an easterly component.

146 For the characterization of Hawaii climate it is useful to divide the year into the cooler,

147 rainier half ("winter", which we define throughout this paper as November through April) and

148 the warmer, drier half ("summer", May through October). Rainfall directly over the main

149 Hawaiian Islands is generally heavier than over adjacent ocean areas due to the strong

150 interaction between the topography and boundary layer flow (e.g., Schroeder 1993). During the

151 dominant trade wind weather patterns generally there is abundant orographic rain along the

6

152 northeastward facing slopes and very pronounced rain shadows over most of the "leeward" (i.e.

153 leeward relative to the mean trade winds) sides of the islands (Lyons 1982). Under the usual

154 TWI conditions there is rarely much deep convective rain over the islands. However, deep

155 convection can occur when the usual TWI pattern is absent. Each winter (and occasionally in

156 summer), the trade wind weather is disrupted several times by spells of more disturbed weather,

157 notably frontal passages or other effects associated with cyclones centered at higher latitudes.

158 On occasion the usual circulation pattern right around Hawaii is strongly perturbed by slowly-

159 moving, closed low pressure circulations (so-called "Kona lows"), which may persist in the

160 vicinity for several days or even longer. These disturbed conditions lead to days without clearly-

161 defined TWI and often feature convective rain. These non-TWI, convective rain events account

162 for much of the total rainfall that falls on the normally dry leeward areas in the islands. In

163 summer, tropical depressions and tropical cyclones can lead to very heavy rainfall events, but

164 the close encounter of such tropical disturbances with the main Hawaiian Islands is relatively

165 infrequent (Chu and Clark 1999). Figure 1a shows schematically some of the key processes

166 governing the rainfall in Hawaii.

167 **3. Observations and model description**

168   In this section, we first describe the data employed to evaluate the model simulation

169 including in-situ and remote sensing observations as well as gridded analyses derived from

170 observations, and then present the model integration performed.

171 *a. Balloon soundings*

172   For the entire 1990-2009 period the National Weather Service conducted twice-daily

173 operational balloon soundings near the eastern and western extremes of the main Hawaiian

174 Islands, namely at Hilo airport on Hawaii Island (which we will refer to here as the "Big Island")

175 and at Lihue Airport on Kauai (Fig. 1b). The soundings include air temperature, humidity and

176 wind speed. Typically there are around 35 levels with data reported below 600 hPa with the

177 density of reports enhanced through the inversion layer itself. The data are available at

178 http://weather.uwyo.edu/upperair/sounding.html.

179 *b. Surface observations*

180   There are several surface weather stations at airports (METAR stations) throughout the

181 islands. We will focus on the detailed observations from METAR stations on each of the four

182 largest islands: Lihue on Kauai, Honolulu on Oahu, Kahului on Maui, and Hilo on the Big

183 Island (see Fig. 1b and the stations denoted by bold type in Table 1). Hourly observations of

184 several variables are taken at each of these stations and the data are available online from the US

185 National Centers for Environmental Information (NCEI) website https://www.ncei.noaa.gov.

186 For comparisons with the model results we will use the station observations of surface air

187 temperature (SAT), surface wind, rainfall and surface specific humidity. The surface wind

188 reported in the METAR data is a 2-minute average of the wind at 10-m height above ground

189 (www.nws.noaa.gov/om/tpb/474body.htm). The hourly METAR data are used to construct daily

190 and monthly means.

191   In addition to the METAR stations, NCEI records daily observations from over 50

192 cooperative weather stations in the main Hawaiian Islands (http://www.prh.noaa.gov/data

193 /HFO/RRMHFO). We used the SAT data (as monthly means reported by the NCEI) from each

194 of the 43 stations for which monthly SAT means were reported for at least 50% of the months

195 during 1990-2009. We also included SAT observations from an additional station at the summit

196 of Mauna Kea on the Big Island that are reported by the Mauna Kea Weather Center

197   (http://mkwc.ifa.hawaii.edu/archive/index.cgi). The network of stations is shown in Fig. 11a and

198   details are given in Table 1.

199   Rainfall amounts are known to exhibit very sharp horizontal contrasts in Hawaii and so

200   characterizing the observed rainfall climatology from observations is challenging. The *Rainfall*

201   *Atlas of Hawaii* project (Giambelluca et al. 2013; Frazier et al. 2015) has tried to compile all

202   available rainfall observations and interpolate them to produce observed monthly-mean rainfall

203   rates at a nominal 250-m resolution over the Hawaiian Islands. The number of rain gauge

204   stations available generally declines over the years but in 2012, for example, monthly data at

205   404 stations (maintained by various organizations) were available. Frazier et al. (2015) discuss

206   results from different kriging approaches for their interpolation using topographic height as a

207   secondary variable. They selected what they judged as the best approach to produce the monthly

208   gridded values that are available at http://rainfall.geography.hawaii.edu (where maps of the

209   station locations can also be found). For our project we aggregated the 250-m observed data to

210   the HRCM 3 km and 1 km grids implemented by using the 'patch' interpolation in NCAR

211   Command Language (https://www.ncl.ucar.edu).

212   The *Rainfall Atlas* does not include hourly data but we will compare the observed and

213   modeled diurnal cycle of rainfall. For this we use hourly rain gauge measurements from the

214   NCEI hourly precipitation dataset and also from the National Weather Service Hydronet which

215   has been recording 15-minute rainfall amounts at stations in Hawaii since 1995

216   (http://www.prh.noaa.gov/hnl/hydro/hydronet/hydronet-data.php). After a data consistency and

217   quality check, we chose 109 stations from the NCEI dataset from 1995 to 2009. During the same

218   time period, there are 64 Hydronet stations available. We performed a Cressman interpolation

219   (Cressman 1959) of the hourly precipitation data onto the Domain 2 3-km grids (following

220   ZWLH). The observed hourly data used are all from 1995-2009; the comparisons presented later

221   concerning the diurnal cycle of rainfall are computed using the model integration for the same

222   15-year period. As an aside, we evaluated our simple Cressman interpolation by comparing our

223   interpolated long term mean rainfall with the more sophisticated results of Frazier et al. (2015)

224   and found generally only small differences.

225   *c. Satellite observations*

226   The MBL structure is measured in situ only by the operational balloon soundings at Hilo

227   and Lihue (see Section 3a above), but Zhang et al. (2012b) reported on the use of satellite

228   remote sensing data in determining the TWI base heights above sea level (TWIBH) in the

229   Hawaiian region. The moisture and temperature gradient across the base of the TWI layer

230   results in a sharp radio refractivity gradient that can be detected by the Global Positioning

231   System (GPS) radio occultation (RO) measurements (e.g., Sokolovskiy et al. 2006; Guo et al.

232   2011; Xie et al. 2012). Zhang et al. (2012b) employed an algorithm to identify the TWIBH from

233   RO soundings (following the method of Guo et al. 2011) and then constructed a climatological

234   map of mean TWIBH for the Hawaiian Region interpolated from all the individual observations

235   from June 2006 to December 2010. Note that the interpolated TWIBH is smoothed to an

236   effective horizontal resolution of ~25 km (this is a particular limitation in representing the

237   inversion base heights over the mountain peaks on Hawaii Island).

238   The Global Precipitation Climatology Project (GPCP) monthly precipitation dataset version

239   2.2 is used to evaluate the precipitation in the outermost domain of the HRCM. This dataset

240   consists of monthly means of precipitation derived from satellite and rain gauge measurements

241   (Adler et al. 2003), and is available at 2.5 degree latitude-longitude resolution. We also

242   employed the monthly mean gridded Tropical Rainfall Measurement Mission (TRMM)

243 precipitation 3B43 product with 0.25 degree resolution based on TRMM and other satellite

244 observations for the time period 1998-2009 (Huffman et al. 2007).

245 *d. Model and integration*

246   A more detailed description of the HRCM can be found in ZWLH. The grid configuration

247 used in the present study is shown in Fig. 1. The model uses "one way nesting" and Domains 1,

248 2 and 3 are integrated with 15, 3, 1 km grids on a Mercator projection. The outer 15 grid points

249 in Domain 1 are used as a buffer zone in which the results are relaxed to values interpolated in

250 time and space from the 6-hour snapshots provided by the NASA MERRA reanalyses

251 (Rienecker et al. 2011). The SST is prescribed and updated daily using the $0.25° \times 0.25°$ NOAA

252 global analysis described by Reynolds et al. (2010, see ZWLH for our treatment of the diurnal

253 variability of the SST). The model integrations started at UTC 00 Jan 01 1990 and ended on

254 UTC 00 Jan 01 2010. We analyze the whole record without discarding a "spin-up" period, since

255 the initial soil moisture and temperature are not crucial to the model performance over the

256 Hawaiian Islands. The model runs in Domains 1, 2 and 3 were performed with time steps of 75,

257 15 and 5 seconds, respectively. The soil moisture and soil temperature at the initial time are

258 taken from the European Centre for Medium-Range Weather Forecasts (ECMWF) Re-Analysis

259 Interim data with a resolution of $0.75° \times 0.75°$ (Dee et al. 2011). The initial conditions for the

260 atmosphere were interpolated from the MERRA global reanalyses $(0.5° \times 0.67°)$.

261   Practical constraints limited us to a single realization of the 20-year period simulated. In

262 fact we can expect this integration to be impacted by random high-frequency internal variability

263 as well as variations under the control of the imposed observed SSTs and lateral boundary

264 conditions (e.g., Cretat et al. 2011). We cannot expect the observed day-to-day evolution of the

265 weather, particularly at small spatial scales, to be reproduced, but, in principle, the seasonal and

266　longer scale interannual variations may be reasonably captured in a single model realization if

267　the control by imposed boundary forcing is sufficiently strong. At least it is meaningful to ask if

268　the model does simulate the interannual variations of the local climate. We show in Section 5

269　that the model does indeed do a reasonable job in simulating the interannual variability on

270　seasonal time-scales.

271　**4. Outermost domain simulation**

272　　　Figure 2 compares our simulated 20-year mean precipitation in Domain 1 with GPCP

273　observations for the same period. In winter, the domain-averaged precipitation is 2.81 mm day^{-1},

274　which is smaller than 3.30 mm day^{-1} indicated by GPCP (Figs. 2a, b). The spatial correlation

275　(SC) between the simulation and GPCP observations computed on the 15 km Domain 1 grid is

276　0.94. In summer (Figs. 2c, d) the domain-averaged simulated precipitation is 2.56 mm day^{-1}, by

277　about 6.5% smaller than the value computed from the GPCP data (2.74 mm day^{-1}). The SC

278　between the simulation and GPCP observations is 0.96. In both seasons the simulated mean

279　precipitation rate is larger than that observed in the ITCZ and less than that observed near, and

280　to the east of, the Hawaiian Islands. Figure 2e shows the monthly time series of domain-

281　averaged precipitation in the HRCM simulation compared with those computed from the GPCP

282　and TRMM rainfall datasets. The main features of the annual cycle as well as the most

283　prominent observed interannual variations (notably over 1997-1998) are reasonably well

284　simulated by the HRCM.

285　　　Figure 3 shows the biases in 20-year means of simulated 500 hPa geopotential height

286　(GHT500) and sea level pressure (SLP) compared with MERRA reanalyses for the same period.

287　The biases are quite small (between -0.2 and 1.0 hPa in SLP and between -15 and 15 m in

288　GHT500) and exhibit only very large-scale gradients (except for the region over the islands

12

289 where the noisy looking results presumably reflect differences in topography and the vertical

290 interpolation/extrapolation between the model and MERRA values). The rather good simulation

291 documented in Figs. 2 and 3 suggests that the regional model with realistic boundary forcing

292 and prescribed SSTs can produce a reasonable representation of the regional-scale fields, even

293 without interior large-scale nudging of model fields as has been done in many other regional

294 climate simulations (e.g., Miguez-Macho et al. 2004; Castro et al. 2005; Lo et al. 2008;

295 Alexandru et al. 2009; Bowden et al. 2012).

296 **5. Intermediate (3 km) domain simulation**

297 *a. Comparison with METAR station observations*

298 The probability density functions (PDFs) of daily mean SAT, daily maximum SAT, daily

299 minimum SAT, daily mean surface specific humidity (Q_2), daily mean surface wind speed and

300 daily rainfall were computed over all days during 1990-2009 from the METAR station data and

301 from the HRCM simulation results at the nearest land grid points to the station locations. The

302 results are shown in Fig. 4 together with the 20-year mean biases (HRCM simulation minus

303 observations). Overall the PDFs in the HRCM simulation and observations are quite similar.

304 The mean SAT biases are less than 0.7°C at all stations. The daily maximum and minimum SAT

305 biases are slightly larger and are in the range of 0.06 to 1.84°C. The bias in humidity at both

306 Lihue and Honolulu is quite small and the simulated PDFs at these stations are similar to the

307 observed. The simulated Q_2 has a dry bias of ~2 g kg^{-1} at both Kahului and Hilo. The HRCM

308 simulation has surface wind speed bias of 1.59 m s^{-1} at Kahului, 0.43 m s^{-1} at Honolulu, and

309 even smaller biases at Hilo and Lihue.

310 The largest mean rainfall bias in the HRCM simulation among the stations is -0.49 mm day$^-$

13

311   [1] for Lihue. The observed distribution of daily rainfall total at each of the stations is rather well

312   captured in the HRCM simulation. The main disagreement is for light rainfall (1-5 mm day^{-1})

313   days which are less frequent at Lihue and Kahului in the simulation than in the observations.

314   The long-term mean seasonal cycle in surface variables is presented as the 20-year means

315   for each calendar month for the same variables (Fig. 5) at the same locations as in Fig. 4.

316   Correlation coefficients of the 12 observed and simulated values for each quantity are also

317   shown in Fig. 5. In each case the seasonal cycle of these surface variables is quite well

318   simulated (with very high correlation coefficients), and even some of the finer details of the

319   observed seasonal cycle (e.g., the May minimum in wind speed at Lihue, Honolulu and Kahului)

320   are captured. The biases in the long-term mean seen earlier in Fig. 4 are apparent here in Fig. 5

321   as well, but the seasonal dependence of these biases is generally modest. Perhaps the most

322   notable systematic seasonal modulation of the model bias is in the SAT at Lihue, Honolulu and

323   Kahului where there is a larger warm bias in summer than in winter.

324   The interannual fluctuations of the surface atmospheric fields are shown as time series from

325   which the long-term mean seasonal cycle has been removed, but in which the long-term annual

326   mean is retained (Fig. 6). Specifically presented in Fig. 6 are 6-month running means of the

327   deseasonalized SAT, wind speed, and rainfall at the four stations. These are compared with the

328   HRCM simulated values at the nearest land grid points. It is noteworthy that the year-to-year

329   fluctuations in all fields at all stations appear to dominate any persistent linear trends, with the

330   exception of surface wind speed at Hilo (discussed further below).

331   The correlation coefficients between these smoothed and deseasonalized SAT time series

332   from HRCM simulation and observations are over 0.9 for all four stations, and the root mean

333   square differences (RMS) between the series are less than 0.75°C. The HRCM simulated

14

334   interannual variations in wind speed appear to be reasonable at Lihue, Honolulu and Kahului

335   (with temporal correlation coefficients of 0.78-0.87) but the result at Hilo is quite anomalous.

336   The observed record shows a strong trend over the 20-year period of decreasing wind speed

337   which is completely absent in the model simulation. We do not have an explanation for this

338   result and speculate that the cause may be inhomogeneity in the observed record, noting that the

339   decrease in the observed wind speed takes place mainly in two steps around 1993 and 2002.

340   The right column of Fig. 6 compares the interannual fluctuations of rainfall simulated by

341   the HRCM with the METAR station observations. Overall the model captures most of the

342   largest fluctuations, notably the wet period around 1995-97 at Lihue, Honolulu and Kahului, and

343   the very dry conditions around 1998-2000 at all four stations. At each station there are also

344   some periods of 6-12 months of significant disagreement particularly in the years since 2004.

345   The correlation coefficients between the observed and modeled values range from 0.45 to 0.68.

346   *b. Rainfall comparisons with gridded analyses- geographical distribution*

347   Figure 7 compares the 20-year mean rainfall over the Hawaiian Islands in the simulation

348   with that in the gridded observational data described in Section 3 for the annual mean, and the

349   summer and winter halves of the year. Promisingly, the model captures all the main qualitative

350   features seen in the complicated rainfall patterns on each of the islands. Specifically one can

351   identify in both observations and model simulation the following features: rainy windward

352   slopes on all islands, the generally dry leeward rain shadow areas, the very wet summit on Kauai,

353   and the two very dry summits on the Big Island (Mauna Kea and Mauna Loa). In both

354   observations and model simulation the long-term mean daily rainfall exceeds 20 mm at some

355   points on the windward sides of east Maui and the Big Island. The spatial correlation coefficient

356   between the gridded observations and model simulation of long-term mean rainfall evaluated on

15

357 the 3 km grid over all the land areas in Hawaii was 0.83 for the annual mean, and 0.84 and 0.79

358 for winter and summer, respectively. The 20-year annual-mean rainfall rate for the land areas of

359 all the Hawaiian Islands is 4.54 mm day^{-1} in the gridded observations and slightly lower (4.49

360 mm day^{-1}) in the HRCM simulation. Compared with the observational analysis, the model mean

361 rainfall over land areas has an overall wet bias of 6% in winter and a dry bias of 12% in summer.

362 While the pattern of overall geographical variation in the climatological rainfall looks

363 reasonable in the model, many particular details are not very well simulated. Some of the most

364 obvious problems occur over Oahu and Maui. The rainfall maximum along the mountains

365 stretching along the east coast of Oahu is too weak in the model. On west Maui the HRCM

366 reproduces the rainfall maximum near the topographic summit, but the rainfall rate there is

367 underestimated by ~5 mm day^{-1} (i.e. by ~40% of the mean observed value). The observed mean

368 rainfall on east Maui has a maximum along the topographic slopes facing northeastward and the

369 area around the summit of Mt. Haleakala is quite dry. In the model simulation the rainfall

370 maximum on east Maui is concentrated on the east end and the southeast-northwest oriented rain

371 maximum along the northeast facing slope in the observations is absent. The heavy rainfall

372 region in the model also penetrates rather close to the mountain summit. These deficiencies over

373 Oahu and Maui have a clear signature in the bias maps (Figs. 7c, f, i) and the pattern of the

374 biases over those islands is similar in winter and summer. The major topographic features on

375 both Oahu and Maui exhibit steep slopes and small horizontal scales. The mountains along the

376 east coast of Oahu are particularly narrow and are significantly smoothed and biased low in the

377 3 km representation. Given that most of the rainfall here is due to topographic interaction with

378 the atmospheric low-level flow, it is not surprising that the model underestimates rainfall along

379 the mountain range. On Maui, as well, the topographic slopes on the mountains in both east

16

380 Maui (Mt. Haleakala) and west Maui are large and the 3 km version of the Maui orography is

381 also considerably smoothed. We have addressed this issue explicitly for Maui with our 1 km

382 "innermost domain" simulation which we will discuss in Section 6 below.

383 On the Big Island the pattern of wet and dry areas is well captured in the model simulation.

384 The model produces a long, narrow maximum in mean rainfall along the west coast of the Big

385 Island corresponding to that observed, but centered slightly more inland (Figs. 7b, e, h). The

386 biggest bias in the simulated mean rainfall on the Big Island evident in Fig. 7 is an

387 overestimation of rainfall along the main topographic slope on the east part of the island,

388 particularly in winter. In winter this bias is as high as ~8 mm day^{-1} representing a ~40%

389 overestimation of local rainfall. The topography on the Big Island is smoother than on the other

390 major Hawaiian Islands so, in contrast to the case for Oahu and Maui, we expect that the

391 resolution of the topography in the 3 km domain is not a major factor in the model bias but the

392 advection scheme for water vapor might play an important role, which will be a topic for a

393 future work.

394 Overall we regard the mean rainfall simulation as successful, but there are model biases at

395 many individual locations that are as much as ~30-40% relative to the Hawaiian rainfall

396 observations and at some exceptional locations, such as the summit of Mt. Haleakala on Maui,

397 can be even larger.

398 *c. Rainfall comparisons with gridded analyses - Interannual variations*

399 Figure 8 presents the individual island mean rainfall values shown as time series from

400 which the long-term mean seasonal cycle has been removed, but with the long-term annual

401 mean retained as in Fig. 6. Results shown have been smoothed with a 6-month running mean,

402 and values for the observations and the HRCM simulation are compared. Just as we saw for

17

403   individual station rainfall observations (Fig. 6), the linear trends are small relative to the other

404   year-to-year variations apparent. The model simulation reproduces the main wet and dry periods

405   seen in the observations. Overall the agreement between the model simulation and observations

406   appears much better for these island-averages (correlation coefficients of 0.66-0.73) than for the

407   individual station values in Fig. 6 (correlation coefficients of 0.45-0.68).

408   Also shown by the black curves in Fig. 8 are estimates of the "local SST" around each

409   island [average of the Reynolds et al. (2010) satellite SST analyses over a 2.5°×2.5° box

410   centered on each of Kauai, Oahu and Maui and over a 4°×4° box around the Big Island. A map

411   of the 20-year trend in observed SSTs is shown in Appendix A]. The local SST appears to have

412   a modest positive correlation with the rainfall over Kauai and Oahu. However, the correlation

413   between SST and island-mean rainfall is very weak for Maui and the Big Island. In general the

414   SST changes are slower than the high-frequency variations in rainfall evident even in the 6-

415   month smoothed curves in Fig. 8.

d. Diurnal rainfall variation

417   The average rainfall in Hawaii exhibits significant diurnal variations which have been

418   documented in many earlier observational studies (e.g., Schroeder et al. 1977; Chen and Nash

419   1994; Sen Roy and Balling 2004; Hartley and Chen 2010). The diurnal variations themselves

420   have a complicated geographical dependence presumably related to the topography on each

421   island. As noted in Section 3b, we have interpolated the hourly rainfall observations archived at

422   NCEI and at Hydronet stations for 1995-2009 onto the 3 km grid, from which 15-year mean

423   statistics were computed. Figure 9a presents maps of the local time at which the diurnal cycle of

424   mean rainfall amount peaks. Figure 9c shows the same quantity for the diurnal cycle of rainfall

425   frequency. Figures 9b, d present comparable values computed from the same 15 years of the

18

426   HRCM simulation. Note that the observations are plotted only over land, while we show model

427   results also over adjacent ocean regions. The peak time is calculated by fitting a 24-hour sine

428   wave to the long-term means calculated for each hour of the day. The results for mean rainfall

429   peak and maximum frequency of rainfall are rather similar (compare Figs. 9a and 9c, or Figs. 9b

430   and 9d). Within each major island there are very significant geographical variations in the phase

431   of the diurnal cycle. There is an overall pattern of early morning peaks (2-6 hours local time -

432   LT) over the windward sides and afternoon peaks (12-15 hours LT) on the leeward sides. This

433   pattern is evident on east Maui, Oahu and Kauai, and even on the rather small island of Molokai.

434   The diurnal rainfall cycle on the Big Island displays even more intricate geographical

435   dependence with a transition from early morning (2-4 hours LT) at the extreme eastern end to

436   late evening (18-22 hours LT) in a substantial band over much of the eastern 1/3 of the island.

437   Most of the western 2/3 of the island has mid-to-late afternoon peaks (14-18 hours LT) with a

438   region of near midnight peaks on the northern tip of the island.

439   The HRCM simulation also shows large variations in diurnal phase within each island. The

440   overall agreement of the simulated patterns with observations is reasonably good, although the

441   model simulation and observations differ in many details. The most notable biases in the HRCM

442   simulation are on the windward sides of Oahu and Kauai where the amount and frequency peaks

443   are around 3 hours later than indicated in the rain gauge observations. Estimates of the

444   amplitude of the climatological diurnal cycle in rainfall (not shown) are also fairly similar in the

445   observational analysis and in the HRCM simulation.

446   *e. Trade wind inversion climatology*

447   The red curves in Figs. 10c, d show the 20-year time series of monthly means of the

448   TWIBH at Lihue and Hilo computed from the twice-daily balloon soundings at each station.

19

449 These monthly averages are computed only using soundings with a well-defined TWI. Details of

450 the definition of TWI and TWIBH we employed are given in Zhang et al. (2012b). The same

451 definitions were used to determine the mean TWIBH in the HRCM simulation and Figs. 10c, d

452 compare the observed (balloon radiosonde) TWIBH and that from the HRCM simulation at the

453 grid points nearest to Lihue and Hilo. The annual and interannual variations in the TWIBH at

454 both stations are simulated reasonably well (with correlation coefficients of 0.71 and 0.74), but

455 the model has a rather persistent low bias of ~100 m.

456   As discussed earlier in Section 3, Zhang et al. (2012b) also estimated TWIBH from satellite

457 radio occultation measurements, which provide the opportunity to evaluate the geographical

458 variations of TWIBH in the model simulation. Figure 10a shows our estimated TWIBH based

459 on these satellite radio occultation observations. This exercise is limited by the relatively few

460 soundings available (see Fig. 10a) and the limited period (2006-2010) covered. The contour map

461 is drawn using an interpolation that lumped together all the data over this period and can be

462 regarded as an estimate of the long-term annual-mean TWIBH (see Zhang et al. 2012b). A

463 comparable long-term mean TWIBH was also computed from the HRCM simulation (Fig. 10b).

464 Note that the model results have been smoothed horizontally to ~25 km resolution to make them

465 somewhat comparable to the observations in equivalent resolution. This explains why the model

466 mean TWIBH shown is only about 2-2.5 km above sea level in areas on the Big Island and Maui

467 where topographic heights are actually higher.

468   The overall low bias of ~100 m noted earlier in the model TWIBH is evident, but the model

469 simulation does capture the overall geographical structure of the TWI around Hawaii that is

470 apparent in observations. Notably the TWIBH is highest near the major islands and is lower on

471 either side, especially in a "bowl" of radius ~100 km, centered near 20ºN and 157ºW (i.e.

20

472 southwest of Oahu and Maui, west of the Big Island).

473 *f. Comparisons with SAT station data*

474 The fact that the HRCM is able to simulate SAT at the METAR stations with biases less

475 than 1°C (Figs. 4, 5, 6) may not be surprising, given that the stations are all near the coast and

476 observed SSTs are prescribed in the model simulation. Here we evaluate the HRCM simulation

477 using the larger database of SAT observations from 44 stations (mainly NOAA cooperative

478 stations) described in Section 3b. This network of stations is shown in Fig. 11a and includes

479 several inland and high altitude locations.

480 Figure 11a presents the 20-year mean bias of the model simulated SAT relative to each

481 station's observations. To produce this comparison we interpolated the HRCM grid values onto

482 the exact station locations by a bilinear interpolation method. The SAT biases over low terrain

483 areas are typically less than 1°C (box 1 in Fig. 11b). However, the biases are larger (1-3°C) over

484 high-elevation areas (Fig. 11b). We then computed a correction based on the differences in

485 elevation between the interpolated model topography and the actual height above sea level at the

486 station locations. The differences in elevation at most stations are less than 100 m, and the

487 largest bias is at the Mauna Kea summit (elevation 4205 m), where the terrain height in the

488 model is about 350 m lower than the actual terrain height (Table 1). The simulated SAT can be

489 adjusted to the real station height by assuming a lapse rate of 6.5°C km^{-1} (Table 1). After

490 applying this correction the SAT bias at the summit of Mauna Kea goes down from 1.7°C to -

491 0.5°C. Overall 50% of 44 stations show a smaller SAT bias after this correction, while 34% of

492 the stations have larger SAT biases. At some stations in box 2 of Fig. 11b (e.g., Kulani Camp 79,

493 Volcano Park HQ 54 and Glenwood Number 2), the negative SAT biases are larger after the

494 elevation correction due to the lower model topography height compared to the real height.

21

495   There is still a 2.2°C bias at Haleakala Ranger Station 338 after applying a 1.1°C adjustment.

496   Figure 11b shows liquid water path (LWP) versus elevation for the surface stations investigated

497   here. Since clouds in Hawaii are typically low clouds (cloud tops below 2.5 km) there is often

498   no ice or mixed phase. The LWP is therefore closely related to the cloud amount and is used

499   here in combination with the elevation of a station to determine whether the station is in the

500   cloud zone in the model ("Box 2" in Fig. 11b) or not ("Box 1"). To explain why all the four

501   windward cloud zone stations have relatively large negative SAT biases, we compared the

502   simulated 20-year net radiation climatology to the retrieved net radiation at the surface by

503   Giambelluca et al. (2014) for the Hawaiian Islands (Fig. 12). The retrieved net radiation is

504   between 80-120 W m^{-2}, while the simulated net radiation is between 50-110 W m^{-2} over the

505   windward sides of the island of Hawaii and Maui (Figs. 12a, b). The total cloud fraction (TCF)

506   and liquid water path are both important factors controlling the net radiation at the surface.

507   There is a slightly higher TCF in the model simulation compared with the TCF retrieved from

508   satellite observations over the windward sides of the islands of Hawaii and Maui (Figs. 12c, d).

509   The overestimated TCF is likely contributing to the negative bias of the net surface radiation in

510   the model. Unfortunately there are no high resolution LWP observations over Hawaii to

511   evaluate the modeled LWP.

512   **6. Innermost domain (1 km) simulation over the Island of Maui**

513   As noted above it seems plausible to attribute much of the deficiencies in the mean rainfall

514   simulation over Oahu and Maui in our intermediate (3 km) domain to the overly smoothed

515   representation of the topography on these islands. We therefore included a 1-km resolution

516   nested innermost domain around Maui in our simulation (Fig. 1). The observed long-term mean

517   rainfall on Maui (Fig. 13a) shows a very uneven distribution and sharp horizontal gradients.

22

518   Mean rainfall exceeds 20 mm day^{-1} at some places on the windward side of Mt. Haleakala in

519   east Maui and near the summit of the mountains in west Maui, but is an order of magnitude less

520   over much of the central parts of the island. The sharp gradients presumably result from

521   interactions of the low-level wind with the Maui's steep topography.

522   Figure 13c shows the 20-year annual-mean rainfall from the intermediate domain (3 km)

523   simulation (i.e. just a detail from Fig. 7b). The deficiencies noted earlier in Section 5 are

524   apparent, notably the rainfall maximum on the eastern side of east Maui is oriented east-west in

525   the simulation rather than southwest-northwest as in the observations. The high rainfall axis

526   penetrates too close to the summit of Mt. Haleakala (elevation 3055 m) which in observations is

527   quite dry. The numbers on Fig. 13a show the locations of NCEI stations from which rainfall data

528   are available (note that this is only a fraction of all rainfall stations used to create the gridded

529   dataset used to produce Fig. 13a). Table 2 shows the observed long-term mean rainfall rate at

530   each station and the simulated values in the 3-km and 1-km domains of the HRCM. On west

531   Maui the model correctly simulates a rainfall maximum near the highest topography, but the

532   peak rainfall there is underpredicted by ~50%.

533   Figure 13b shows the simulated mean rainfall rates in the 1-km resolution domain

534   simulation. The great improvement in the pattern of rainfall compared with the simulation in the

535   3-km resolution domain is evident. The results for the individual NCEI stations in Table 2 are

536   almost all improved substantially in the 1-km simulation. Notably at station #1 the bias of more

537   than 300% in the 3-km simulation is reduced to 33% in the 1-km resolution simulation.

538   **7. Discussion and conclusions**

539   We integrated a triply-nested version of the HRCM for 20 years which was forced by global

540   reanalysis data and observed SSTs. The horizontal resolution is 15 km over an extensive ocean

23

541   area in the central equatorial and North Pacific, 3 km for the Hawaiian Islands and adjacent

542   oceans, and 1 km for the island of Maui and surroundings. The basic features of the regional

543   scale climatology simulated in the HRCM outermost domain including the mean location of the

544   ITCZ and long-term mean SLP patterns are reasonably well reproduced by the model.

545   The intermediate 3-km resolution domain results were compared with a wide variety of

546   local station and other high-resolution observations in order to evaluate how well the HRCM

547   can simulate the fine structure of Hawaiian microclimates. Near the coasts, the model long-term

548   mean SAT biases relative to station observations are almost everywhere less than 1°C -

549   agreement which presumably is largely ordained by the prescription of observed SSTs in the

550   adjacent ocean regions. At inland locations the model simulated SAT is less directly constrained

551   by the SSTs and model biases in SAT in the 1-2°C range are common at many locations and the

552   bias exceeds 3°C at one station (Fig. 11). The simulated long-term mean rainfall was compared

553   with observations at some individual stations and with a gridded analysis over all land areas

554   derived from a sophisticated optimal interpolation of several hundred station observations. The

555   overall geographical and seasonal patterns of rainfall over the islands are captured reasonably

556   well in the HRCM simulation. The spatial correlation coefficient between interpolated

557   observations and model simulation of long term mean rainfall evaluated on 3 km grids over all

558   the land areas in Hawaii was 0.79-0.84 depending on the season considered. However, we find

559   model biases at individual locations that are ~30-40% relative to the interpolated observations.

560   Overall, the HRCM biases in simulated climatological SAT and rainfall at individual locations

561   over the Hawaiian Islands seem fairly modest.

562   More detailed analysis of rain gauge data and model output showed that the HRCM

563   simulates a quite realistic diurnal cycle of rainfall. This result is gratifying as this aspect of the

564 circulation is generated internally within the model and is not strongly controlled by the

565 prescribed boundary conditions.

566   We used objective criteria to classify any observed or simulated atmospheric sounding as

567 representing typical TWI conditions or not, and found a TWI frequency of about 80% in both

568 observations and the model simulation. The TWI periods of the record were analyzed to create

569 the climatology of TWI height in the model which was compared to TWI statistics from balloon

570 soundings and GPS satellite profiles. While there is basic agreement in the geographical and

571 seasonal variations of the mean TWI in the observations and model simulation, the HRCM does

572 display a fairly consistent low bias of ~100 m in the TWIBH.

573   We also analyzed aspects of the interannual variations in the simulated rainfall, SAT and

574 surface wind speed. The overall strength of interannual fluctuations in rainfall is reasonably well

575 captured in the simulations. The detailed time series of the modeled rainfall, SAT and surface

576 wind speed over the 20 year period are reasonably close to observations (Figs. 6 and 8). The

577 most striking feature of the observed rainfall records, namely the heavy rain in 1995-96

578 followed by a protracted period of below-average rainfall until 2001, is reproduced to some

579 extent in the HRCM simulation. The observed time series over the period showed significant

580 variability on a range of time-scales and in none of the records did consistent long-term trends

581 appear to be the dominant contribution to interannual variability. Nonetheless we did examine

582 the 20-year linear trends in the observed and simulated SAT and rainfall fields and found some

583 degree of agreement. Any 20 year trends in regional atmospheric conditions would be forced

584 primarily by the 20 year trends in SST in the Pacific basin, and those SST trends are up to

585 ~0.1°C yr^{-1} locally and have substantial geographical structure. These 20-year SST trends are

586 likely dominated by just sampling of low frequency natural variability such as the Pacific

587 Decadal Oscillation (PDO) and have little resemblance to the SST warming patterns anticipated

588 over longer timescales from anthropogenic climate forcing.

589   Ideally we would like to show that the statistical properties of the HRCM simulation (such

590 as long-term mean rainfall rates) have converged at the grid resolution employed. As for most

591 comprehensive climate simulations we do not have the luxury of demonstrating numerical

592 convergence of our solutions or of being able to confidently say how much any remaining

593 deficiencies in the simulations can be ascribed to the finite grid resolution of the model.

594 However on the Big Island the relatively smooth geographical patterns in both observed and

595 modeled mean rainfall suggest that the 3 km horizontal grid spacing in our intermediate domain

596 may be adequate. However the topography on each of Maui, Oahu and Kauai is overall steeper

597 than on the Big Island and aspects of the topography seem not adequately resolved even in 3 km

598 grids. As part of this study we included an innermost domain with 1 km horizontal resolution

599 over the island of Maui. The results in the 1-km simulation showed substantial improvement of

600 the simulated mean rainfall climatology. This improvement can be plausibly explained by the

601 better resolution of the topography on the 1-km grids. Our planned future work includes

602 exploring simulations with enhanced resolution model grids over Oahu and Kauai.

603   Despite some remaining biases, the overall success of the HRCM in reproducing Hawaiian

604 microclimate over the 20-year historical period considered here gives us confidence that the

605 model is suitable for application to fine spatial resolution climate change projections for the

606 Hawaiian Islands. Part II of this work will present the results from HRCM simulations designed

607 as a projection for global climate conditions of the late 21st century. Results of the simulations

608 reported in this two-part paper will be publically available at the Asia-Pacific Data-Research

609 Center of the University of Hawaii at Manoa (http://apdrc.soest.hawaii.edu/).

Appendix

Low Frequency SST Variability

618

619

620 The observed and modeled rainfall time series shown in Figs. 6 and 8 reveal significant

621 variability from year-to-year as well as at decadal and possibly even longer time scales.

622 Measures of observed state-wide rainfall show correlations with the phase of the Pacific

623 Decadal Oscillation (PDO; e.g. Chu and Chen, 2005) and it is reasonable to suppose that the

624 changes in Hawaii rainfall on long time scales are largely driven by the regional-to-basin scale

625 SST variations associated with the PDO. There may also be a consistent warming trend in the

626 SST variations that represent the effects of anthropogenically forced global warming. The actual

627 trend in the SST (Fig. A1) over our period of interest has little resemblance to the SST warming

628 pattern anticipated over longer timescales from anthropogenic climate forcing, and is probably

629 best regarded as resulting primarily from the 20-year sample of low frequency natural variability

630 such as the PDO.

References

631

632 Adler, R. F., and Coauthors 2003: The Version 2 Global Precipitation Climatology Project

633   (GPCP) Monthly Precipitation Analysis (1979-Present). *J. Hydrometeor.*, **4,** 1147-1167**.**

634 Alexandru, A., R. de Elia, R. Laprise, L. Separovic, and S. Biner, 2009: Sensitivity study of

635   regional climate model simulations to large-scale nudging parameters. *Mon. Wea. Rev.*, **137**,

636   1666–1685, doi: 10.1175/2008MWR2620.1.

637 Bowden, J. H., T. L. Otte, C. G. Nolte, and M. J. Otte, 2012: Examining interior grid nudging

638   techniques using two-way nesting in the WRF model for regional climate modeling. *J.*

639   *Climate*, **25**, 2805–2823, doi: 10.1175/JCLI-D-11-00167.1.

640 Cao, G., T. W. Giambelluca, D. E. Stevens, and T. A. Schroeder, 2007: Inversion variability in

641   the Hawaiian trade wind regime. *J. Climate*, **20**, 1145–1160, doi: 10.1175/JCLI4033.1.

642 Castro, C. L., R. A. Pielke Sr., and G. Leoncini, 2005: Dynamical downscaling: Assessment of

643   value retained and added using the Regional Atmospheric Modeling System (RAMS). *J.*

644   *Geophys. Res.*, **110**, D05108, doi: 10.1029/2004JD004721.

645 Chen, Y.-L., and A. J. Nash, 1994; Diurnal variations of surface airflow and rainfall frequencies

646   on the island of Hawaii, *Mon. Weather Rev.*, **122**, 34–56.

647 Chu, P.-S., and H. Chen, 2005: Interannual and interdecadal rainfall variations in the Hawaiian

648   Islands. *J. Climate*, **18**, 4796–4813, doi: 10.1175/JCLI3578.1.

649 Chu, P.-S., and J. D. Clark, 1999: Decadal variations of tropical cyclone activity over the

650   Central North Pacific. *Bull. Amer. Meteor. Soc.*, **80**, 1875–1881.

651 Cressman, G. P., 1959: An operational objective analysis system. *Mon. Wea. Rev.*, **87**, 367–374.

652 Cretat, J. C., M. B. Pohl, and Y. Richard, 2011: Quantifying internal variability in a regional

653   climate model: a case study for Southern Africa. *Clim. Dyn.*, **37**, 1335-1356, doi:

654   10.1007/s00382-011-1021-5.

655 Dee, D. P., and Coauthors, 2011: The ERA-Interim reanalysis: Configuration and performance

656   of the data assimilation system. *Quart. J. Roy. Meteor. Soc.*, **137**, 553–597, doi:

657   10.1002/qj.828.

658 Frazier, A. G., Giambelluca, T. W., Diaz, H. F. and Needham, H. L., 2015: Comparison of

659   geostatistical approaches to spatially interpolate month-year rainfall for the Hawaiian Islands.

660   *Int. J. Climatol*, doi: 10.1002/joc.4437.

661 Fu, C., and Coauthors, 2005: Regional climate model intercomparison project for Asia. *Bull.*

662   *Amer. Meteor. Soc.*, **86**, 257–266, doi: 10.1175/BAMS-86-2-257.

663 Giambelluca, T.W., Q. Chen, A.G. Frazier, J.P. Price, Y.-L. Chen, P.-S. Chu, J.K. Eischeid, and

664   D.M. Delparte, 2013: Online Rainfall Atlas of Hawai'i. *Bull. Amer. Meteor. Soc.* **94**, 313-316,

665   doi: 10.1175/BAMS-D-11-00228.1.

666   Giambelluca, T. W., and Coauthors, 2014: Evapotranspiration of Hawai'i. Final report

667   submitted to the U.S. Army Corps of Engineers—Honolulu District, and the Commission on

668   Water Resource Management, State of Hawai'i.

669   Guo, P., Y.-H. Kuo, S. V. Sokolovskiy, and D. H. Lenschow, 2011: Estimating atmospheric

670   boundary layer depth using COSMIC radio occultation data, *J. Atmos. Sci.*, **68**, 1703–1713,

671   doi: 10.1175/2011JAS3612.1.

672   Harter, D. E. V., S. D. H. Irl, B. Seo, M. J. Steinbauer, R. Gillespie, K. A. Triantis, J.-M.

673   Fernández-Palacios, and C. Beierkuhnlein, 2015: Impacts of global climate change on the

674   floras of oceanic islands – Projections, implications and current knowledge. *Perspect. Plant*

675   *Ecol. Evol. Syst.,* **17**, 160-183, doi: 10.1016/j.ppees.2015.01.003.

676   Hartley, T. M., and Y.-L. Chen, 2010: Characteristics of summer trade wind rainfall over Oahu.

677   *Wea. Forecasting*, **25**, 1797–1815, doi: 10.1175/2010WAF2222328.1.

678   Hostetler, S. W., J. R. Alder, and A. M. Allan, 2011: Dynamically downscaled climate

679   simulations over North America: Methods, evaluation and supporting documentation for

680   users: U.S. Geological Survey Open-File Report 2011-1238, 64 pp.

681   Huffman, G. J., R. F. Adler, D. T. Bolvin, G. Gu, E. J. Nelkin, K. P. Bowman, E. F. Stocker,

682   and D. B. Wolff, 2007: The TRMM multi-satellite precipitation analysis: Quasi-global,

683   multi-year, combined-sensor precipitation estimates at fine scale. *J. Hydrometeor.*, **8**, 33-55,

684   doi: 10.1175/JHM560.1.

685   Kendon, E. J., N. M. Roberts, H. J. Fowler, M. J. Roberts, S. C. Chan, and C. A. Senior, 2014:

686   Heavier summer downpours with climate change revealed by weather forecast resolution

687   model. *Nature Clim. Change*, doi: 10.1038/NCLIMATE2258.

688   Laprise, R., D. Caya, M. Giguère, G. Bergeron, H. Côté, J.-P. Blanchet, G. J. Boer, and N. A.

689   McFarlane, 1998: Climate and climate change in western Canada as simulated by the

690   Canadian Regional Climate Model. *Atmos.–Ocean*, **36**, 119–167.

691   Leong, J.-A., and Coauthors, 2014: Ch. 23: Hawai'i and U.S. affiliated Pacific islands. *Climate*

692   *Change Impacts in the United States: The Third National Climate Assessment*, J. M. Melillo,

693   Terese (T.C.) Richmond, and G. W. Yohe, Eds., U.S. Global Change Research Program,

694   537-556, doi: 10.7930/J0W66HPM.

695   Lo, J. C.-F., Z.-L. Yang, and R. A. Pielke Sr., 2008: Assessment of three dynamical

696   downscaling methods using the Weather Research and Forecasting (WRF) model. *J. Geophys.*

697   *Res.*, **113**, D09112, doi: 10.1029/2007JD009216.

698   Lyons, S. W., 1982: Empirical orthogonal function analysis of Hawaiian rainfall. *J. Appl.*
699   *Meteor.*, **21**, 1713–1729.

700   Mahoney, K., M. Alexander, J. D. Scott, and J. Barsugli, 2013: High-resolution downscaled
701   simulations of warm-season extreme precipitation events in the Colorado Front Range under
702   past and future climates. *J. Climate*, **26**, 8671–8689, doi: 10.1175/JCLI-D-12-00744.1.

703   Mearns, L. O, and Coauthors, 2012: The North American Regional Climate Change Assessment
704   Program: Overview of Phase I results. *Bull. Amer. Meteor. Soc.*, **93**, 1337–1362, doi:
705   10.1175/BAMS-D-11-00223.1.

706   Miguez-Macho, G., G. L. Stenchikov, and A. Robock, 2004: Spectral nudging to eliminate the
707   effects of domain position and geometry in regional climate model simulations. *J. Geophys.*
708   *Res.*, **109**, D13104, doi: 10.1029/2003JD004495.

709   Morel, B., B. Pohl, Y. Richard, B. Bois, and M. Bessafi, 2014: Regionalizing rainfall at very
710   high resolution over La Réunion Island using a regional climate model. *Mon. Wea. Rev.*, **142**,
711   2665–2686, doi: 10.1175/MWR-D-14-00009.1.

712   Pérez, J.C., J. P. Díaz, A. González, J. Expósito, F. Rivera-López, and D. Taima, 2014:
713   Evaluation of WRF parameterizations for dynamical downscaling in the Canary Islands. *J.*
714   *Climate*, **27**, 5611–5631, doi: 10.1175/JCLI-D-13-00458.1.

715   Prein, A.F., and Coauthors, 2015: A review on regional convection-permitting climate
716   modeling: Demonstrations, prospects, and challenges, *Rev. Geophys.*, **53**, 323–361, doi:
717   10.1002/2014RG000475.

718   Rasmussen, R., and Coauthors, 2014: Climate change impacts on the water balance of the
719   Colorado Headwaters: High-resolution regional climate model simulations. *J. Hydrometeor.*,
720   **15**, 1091–1116, doi: 10.1175/JHM-D-13-0118.1.

721   Reynolds, R. W., C. L. Gentemann and G. K. Corlett, 2010: Evaluation of AATSR and TMI
722   Satellite SST data. *J. Climate*, **23**, 152-165, doi: 10.1175/2009JCLI3252.1.

723   Rienecker, M. M., and Coauthors, 2011: MERRA: NASA's Modern-Era Retrospective Analysis
724   for Research and Applications. *J. Climate*, **24**, 3624–3648, doi: 10.1175/JCLI-D-11-00015.1.

725   Rummukainen, M., 2010: State-of-the-art with regional climate models. *WIREs Clim. Change*, **1**,
726   82–96, doi: 10.1002/wcc.8.

727   Schroeder, T. A., 1993: Climate controls. Prevailing Trade Winds: Weather and Climate in
728   Hawai'i, M. Sanderson, Ed., University of Hawai'i Press, 12–36.

729   ——, B. Kilonsky, and B. Meisner, 1977: Diurnal variation in rainfall and cloudiness. Water

730   Resources Research Center Tech Rep. 112, 67 pp.

731 Sen Roy, S., and R. C. Balling, 2004: Analysis of Hawaiian diurnal rainfall patterns. *Theor.*
732   *Appl. Climatol.*, **79**, 209-214.

733 Skamarock, W.C., and Coauthors, 2008: A description of the Advanced Research WRF version
734   3. NCAR Tech. Note NCAR/TN-4751STR, 113pp, doi: 10.5065/D68S4MVH.

735 Sokolovskiy, S., Y.-H. Kuo, C. Rocken, W. S. Schreiner, D. Hunt, and R. A. Anthes, 2006:
736   Monitoring the atmospheric boundary layer by GPS radio occultation signals recorded in the
737   open-loop mode, *Geophys. Res. Lett*., **33**, L12813, doi:10.1029/2006GL025955.

738 Taylor, K. E., R. J. Stouffer, and G. A. Meehl, 2012: An overview of CMIP5 and the experiment
739   design. *Bull. Amer. Meteor. Soc.*, **93**, 485–498, doi: 10.1175/BAMS-D-11-00094.1.

740 Wang, Y., L.R. Leung, J. L. McGregor, D.-K. Lee, W.-C. Wang, Y.-H. Ding, and F. Kimura,
741   2004: Regional climate modeling: Progress, challenges and prospects. *J. Meteor. Soc.*
742   *Japan*, **82**, 1599-1628.

743 Xie, F., D. L. Wu, C. O. Ao, A. J. Mannucci, and E. R. Kursinski, 2012: Advances and
744   limitations of atmospheric boundary layer observations with GPS occultation over southeast
745   Pacific Ocean, *Atmos. Chem. Phys*., **12**, 903-918, doi: 10.5194/acp-12-903-2012.

746 Zhang, C. X., Y. Wang, and K. Hamilton, 2011: Improved representation of boundary layer
747   clouds over the Southeast Pacific in WRF-ARW using a modified Tiedtke cumulus
748   parameterization scheme. *Mon. Wea. Rev.*, **139**, 3489–3513, doi: 10.1175/MWR-D-10-
749   05091.1.

750 Zhang, C. X., Y. Wang, A. Lauer, and K. Hamilton, 2012a: Configuration and evaluation of the
751   WRF model for the study of Hawaiian regional climate. *Mon. Wea. Rev.*, **140**, 3259–3277.
752   doi: 10.1175/MWR-D-11-00260.1.

753 ——, Y. Wang, A. Lauer, K. Hamilton, and F. Xie, 2012b: Cloud base and top heights in the
754   Hawaiian region determined with satellite and ground-based measurements, *Geophys. Res.*
755   *Lett.*, **39**, L15706, doi:10.1029/2012GL052355.

756

Figure captions

Figure 1. (a) Model domains and synoptic patterns most relevant to weather and climate in the
Hawaiian Islands. (b) The terrain heights and the locations of the METAR stations employed
here. (c) Domain 3 (1 km horizontal resolution).

Figure 2. The 20-year mean winter precipitation in (a) the GPCP gridded observations, and (b)
HRCM 15 km simulation. (c) as in (a) but for summer. (d) as in (b) but for summer. (e) The
time series for the simulated monthly mean rainfall averaged over the whole domain in the
model simulation (dashed blue), the GPCP observations (red) and the TRMM observations
(black). SC means spatial correlation coefficient.

Figure 3. The 20-year mean geopotential height at 500 hPa (GHT500) (shaded, m) and mean sea
level pressure (SLP) (contour, hPa) biases (HRCM simulation minus MERRA reanalysis data)
for (a) winter, and (b) summer.

Figure 4. PDFs of the daily values over the time period 1990-2009 of (left to right): daily mean
surface air temperature (SAT), daily maximum SAT, daily minimum SAT, daily mean
surface specific humidity (Q_2), daily mean surface wind speed at (top to bottom) Lihue,
Honolulu, Kahului and Hilo. Red lines show station observations and blue lines are for the
HRCM 3 km simulation at nearest land grid points to stations. The simulated long-term mean
biases (HRCM simulation minus observations) for each variable are also shown in the figure.
The rightmost column is the daily rainfall histogram for each station with colored shading
showing the observed values and the hatching showing the result for the HRCM 3 km
simulation. The bin width for SAT is 1°C, for surface specific humidity is 1 g kg^{-1}, for wind
speed is 1 m s^{-1}, and uneven for rainfall as shown by the tick marks.

Figure 5. The 20-year mean seasonal cycle for surface air temperature (SAT), wind speed and
rainfall at Lihue, Honolulu, Kahului and Hilo, respectively. The red line is for station
observations, and the blue line is for the HRCM 3 km simulation at the nearest land grid
points. The correlation coefficient between the two curves, C, is shown at upper right corner
of each panel.

Figure 6. The time series of mean surface air temperature (SAT), wind speed and rainfall at
Lihue, Honolulu, Kahului and Hilo. Quantities shown are 6-month running-means. Red
curves are for the station observations, and blue is for the HRCM 3 km simulation at the land
grid point nearest to the station. 'RMS' is the mean root mean square difference between
model and observational curves, and 'C' is the correlation coefficient between the two curves.
The least squares linear regression trends over the 20 years are also shown in each panel.

Figure 7. (a) The observed 20-year annual mean rainfall based on several hundred measurement
stations (see text for details). (b) The simulated annual mean rainfall from the 3 km HRCM

792   simulation. 'SC' is the spatial correlation over the land calculated for 3 km grids. Also shown

793   are the averaged rainfall amounts (mm d^{-1}) over all land areas. (c) The model bias (model

794   minus observations). The observations, model results and the model biases for winter and

795   summer are shown in (d-f) and (g-i), respectively.

796   Figure 8. The interannual variations of the rainfall (red is for observations; blue is for the

797   HRCM 3 km simulation) and local SST (black) for the Islands of Kauai, Oahu, Maui and

798   Hawaii. C1 denotes the correlation coefficient between local SST and observed rainfall. C2

799   denotes the correlation coefficient between observed and simulated rainfall. The trends are

800   also shown in the figure.

801   Figure 9. Phase of the diurnal harmonic of long-term mean annual-mean rainfall. Specifically

802   shown are the local time (LT) peak of the diurnal (24-hour) harmonic of the mean rainfall

803   rate (a, b) and rainfall frequency (c, d). Results for our gridded observations over land are in

804   (a, c) and those for the HRCM simulation are in (b, d).

805   Figure 10. The trade wind inversion base height (TWIBH) derived from the COSMIC

806   observations (a) and the HRCM simulation (b). The black dots in (a) are the locations of the

807   observed profiles from COSMIC. The time-series of monthly mean of the TWIBH computed

808   from balloon soundings at Lihue and Hilo are shown by the red curves in (c) and (d),

809   respectively. The values from the HRCM simulation are shown by the blue curves. The

810   correlation coefficient between the observed and modeled time series is shown in the upper

811   right corner of each panel.

812   Figure 11. The distribution map for the 20-year mean surface air temperature (SAT) bias

813   (HRCM simulations minus observations) over the Hawaiian Islands (a). The temperature

814   biases (e.g., "1:2" means "1 to 2") for each station related to liquid water path (LWP) and

815   topography are also shown (b). Some station names are marked in the figures. K is degrees in

816   Kelvin. Box 1 includes the low topography stations, and Box 2 includes the stations that are

817   in the cloud zone in the model.

818   Figure 12. The retrieved net radiation at the surface (a) and total cloud fraction (c) climatology

819   by Giambelluca et al. (2014), and the model simulated climatology of net surface radiation

820   (b) and total cloud fraction (d).

821   Figure 13. The 20-year mean rainfall in observations (a), the HRCM 1 km simulation (b) and

822   the HRCM 3 km simulation (c). The numbers in (a) are the NCEI observational stations

823   listed in Table 2.

824   Figure A1. The trend in the Reynolds (2010) observed sea surface temperatures (SSTs) over the

825   time period 1990-2009 based on a linear regression of the monthly mean values at each grid

826   point. The trend is expressed in Kelvin (K) over 20 years.

827 Table 1. Long-term mean surface air temperature (SAT) from the METAR (in bold) and other
828   surface temperature stations (some of the stations are shown in Fig.11). Also shown is the
829   difference, ΔSAT, with the model simulation using values interpolated horizontally to the
830   station location. ΔElev is the elevation difference between the model-interpolated
831   topography and the actual station elevation. "SAT Adj" is the air temperature adjustment
832   applied to the model result to account for this elevation bias. The last column shows the
833   ΔSAT after the elevation-related adjustment.

Station Name	Lat (N)	Lon (E)	Elev (m)	ΔElev (m)	SAT (°C)	ΔSAT (°C)	SAT Adj (°C)	ΔSAT After Adj. (°C)
Camp Erdman	21.6	-158.2	2.1	182.9	24.1	-1.9	1.2	-0.8
Glenwood Number 2	19.5	-155.1	670.6	-75.9	19.5	-1.1	-0.5	-1.6
Haleakala Ranger Station 338	20.8	-156.2	2121.4	168.7	12.5	-3.3	1.1	-2.2
Hana Airport	20.8	-156.0	22.9	55.6	23.3	-0.3	0.4	0.0
Hawaii Vol National Park HQ 54	19.4	-155.2	1210.4	-72.5	16.5	-1.6	-0.5	-2.0
Hilo International Airport	**19.7**	**-155.1**	**11.6**	**-2.5**	**23.4**	**0.7**	**-0.0**	**0.7**
Honolulu Observatory	21.3	-158.0	0.9	0.0	24.5	-0.2	0.0	-0.2
Honolulu International Airport	**21.3**	**-157.9**	**2.5**	**3.0**	**25.5**	**-0.7**	**0.0**	**-0.7**
Kahoolawe	20.5	-156.6	365.8	-104.3	21.9	0.2	-0.7	-0.5
Kahului Airport	**20.9**	**-156.4**	**15.5**	**23.1**	**24.4**	**-0.6**	**0.2**	**-0.4**
Kailua 446	20.9	-156.2	213.4	7.7	20.0	1.2	0.1	1.3
Kainaliu	19.5	-155.9	457.2	37.9	20.8	-0.1	0.2	0.2
Kanalohuluhulu	22.1	-159.6	1097.3	-111.0	15.0	1.4	-0.7	0.6
Kaneohe	21.4	-157.8	14.6	34.4	25.1	-1.2	0.2	-1.0
Kapalua West Maui Airport	21.0	-156.7	73.2	62.2	24.2	-0.9	0.4	-0.5
KE Ahole Point	19.7	-156.1	6.1	11.5	24.9	-0.3	0.1	-0.2
Kihalani	20.0	-155.2	301.8	-42.6	21.7	-0.3	-0.3	-0.6
Kii Kahuku 911	21.7	-157.9	7.6	4.6	24.2	-0.3	0.0	-0.3
Kula Branch Station	20.8	-156.3	944.9	72.1	17.8	-0.4	0.5	0.1
Kula Hospital 267	20.7	-156.4	923.5	207.4	17.4	-1.2	1.3	0.2
Kulani Camp 79	19.5	-155.3	1575.8	-32.8	12.8	-0.4	-0.2	-0.6
Lanai Airport	20.8	-156.9	396.2	-42.3	21.9	-0.7	-0.3	-1.0
Lihue Airport	**22.0**	**-159.3**	**54.0**	**-19.1**	**24.3**	**-0.7**	**-0.1**	**-0.8**
Makaha Country Club	21.5	-158.2	76.2	158.6	24.1	-1.8	1.0	-0.7
Makena Golf Course	20.6	-156.4	26.8	83.8	24.0	-0.4	0.5	0.2
Makaweli	21.9	-159.6	42.7	-9.8	24.5	-1.2	-0.1	-1.2
Manoa LYON ARBO	21.3	-157.8	152.4	106.4	22.7	-0.7	0.7	-0.0
Mauna Loa Slope OBS 39	19.5	-155.6	3398.5	96.4	8.0	-1.8	0.6	-1.2
Molokai Airport	21.1	-157.1	135.0	9.0	23.7	-0.9	0.1	-0.8
Naalehu	19.0	-155.6	245.7	-77.8	22.7	-0.1	-0.5	-0.6
OHE'O	20.6	-156.0	28.0	2.4	24.0	-0.1	0.0	-0.1
Opihihale	19.3	-155.9	414.5	70.9	20.9	0.2	0.5	0.7
Princeville Ranch	22.2	-159.5	66.1	-33.2	23.5	-0.1	-0.2	-0.4
Puukolii	20.9	-156.7	128.0	37.2	24.0	-0.5	0.2	-0.3
Puukohola Heiau	20.0	-155.8	40.5	39.0	23.4	1.2	0.3	1.4
Puu Manawahua	21.4	-158.1	509.9	-288.8	21.2	1.1	-1.9	-0.7
Sea Mountain	19.1	-155.5	24.4	-6.2	23.6	0.4	-0.0	0.4
South Kona 2	19.1	-155.8	719.3	1.1	19.6	-0.2	0.0	-0.2
Upper Wahiawa	21.5	-158.0	306.9	-52.0	22.1	-0.3	-0.3	-0.7
Waikiki	21.3	-157.8	3.0	18.5	25.1	-0.7	0.1	-0.6
Waimanalo Experimental Farm	21.3	-157.7	19.5	43.1	24.2	-0.7	0.3	-0.5
Waimea Arboretum 892	21.6	-158.1	12.5	121.8	23.7	-1.1	0.8	-0.3
Waimea 947	22.0	-159.7	6.1	20.3	23.9	-0.0	0.1	0.1
Mauna Kea Summit	19.8	-155.5	4205.0	-350.0	2.2	1.7	-2.3	-0.5

834 Table 2. The NCEI rainfall stations (location of each station is shown in Fig.13a) over the Island

835 of Maui with the observed and HRCM-simulated long-term mean rainfall rates.

Station	Latitude (N)	Longitude (E)	Elevation (m)	OBS (mm/day)	3 km simulation			1 km simulation		
					Mean (mm/day)	Bias (mm/day)	Bias (%)	Mean (mm/day)	Bias (mm/day)	Bias (%)
1	20.75	-156.23	2122	3.2	14.9	*11.8*	**369**	4.2	*1.1*	**33**
2	20.85	-156.33	329	3.0	2.0	*-1.0*	**-34**	2.7	*-0.3*	**-10**
3	20.92	-156.33	98	3.0	2.1	*-0.9*	**-29**	3.1	*0.1*	**2**
4	20.98	-156.65	67	2.4	1.6	*-0.8*	**-34**	2.8	*0.4*	**17**
5	20.88	-156.42	16	1.1	0.9	*-0.2*	**-18**	1.1	*-0.0*	**-4**
6	20.88	-156.20	213	8.3	5.8	*-2.5*	**-30**	7.6	*-0.7*	**-8**
7	21.18	-156.97	9	2.9	2.0	*-0.9*	**-32**	2.1	*-0.8*	**-26**
8	20.95	-156.67	73	1.9	1.1	*-0.8*	**-41**	1.8	*-0.1*	**-6**
9	20.75	-156.32	945	1.5	2.2	*0.7*	**43**	1.6	*0.1*	**4**
10	20.70	-156.35	924	2.0	3.2	*1.2*	**58**	1.6	*-0.4*	**-18**
11	21.02	-156.60	107	2.6	1.8	*-0.8*	**-32**	2.1	*-0.5*	**-21**
12	20.69	-156.03	28	5.7	5.2	*-0.5*	**-9**	6.4	*0.6*	**11**
13	20.78	-156.27	1256	3.7	6.3	*2.6*	**69**	2.9	*-0.9*	**-23**
14	20.80	-156.12	383	13.6	8.0	*-5.6*	**-41**	14.1	*0.6*	**4**
15	20.90	-156.37	52	2.0	1.3	*-0.6*	**-32**	1.9	*-0.1*	**-5**
16	20.92	-156.67	128	1.7	1.1	*-0.6*	**-36**	1.3	*-0.4*	**-25**
17	20.88	-156.40	27	1.5	1.0	*-0.5*	**-32**	1.3	*-0.2*	**-14**
18	20.63	-156.38	579	2.1	1.3	*-0.8*	**-38**	1.6	*-0.4*	**-20**
19	20.90	-156.50	98	2.2	1.1	*-1.1*	**-51**	1.3	*-1.0*	**-43**
20	20.93	-156.52	104	2.9	1.6	*-1.4*	**-47**	1.8	*-1.1*	**-38**

Figure 1. (a) Model domains and synoptic patterns most relevant to weather and climate in the Hawaiian Islands. (b) The terrain heights and the locations of the METAR stations employed here. (c) Domain 3 (1 km horizontal resolution).
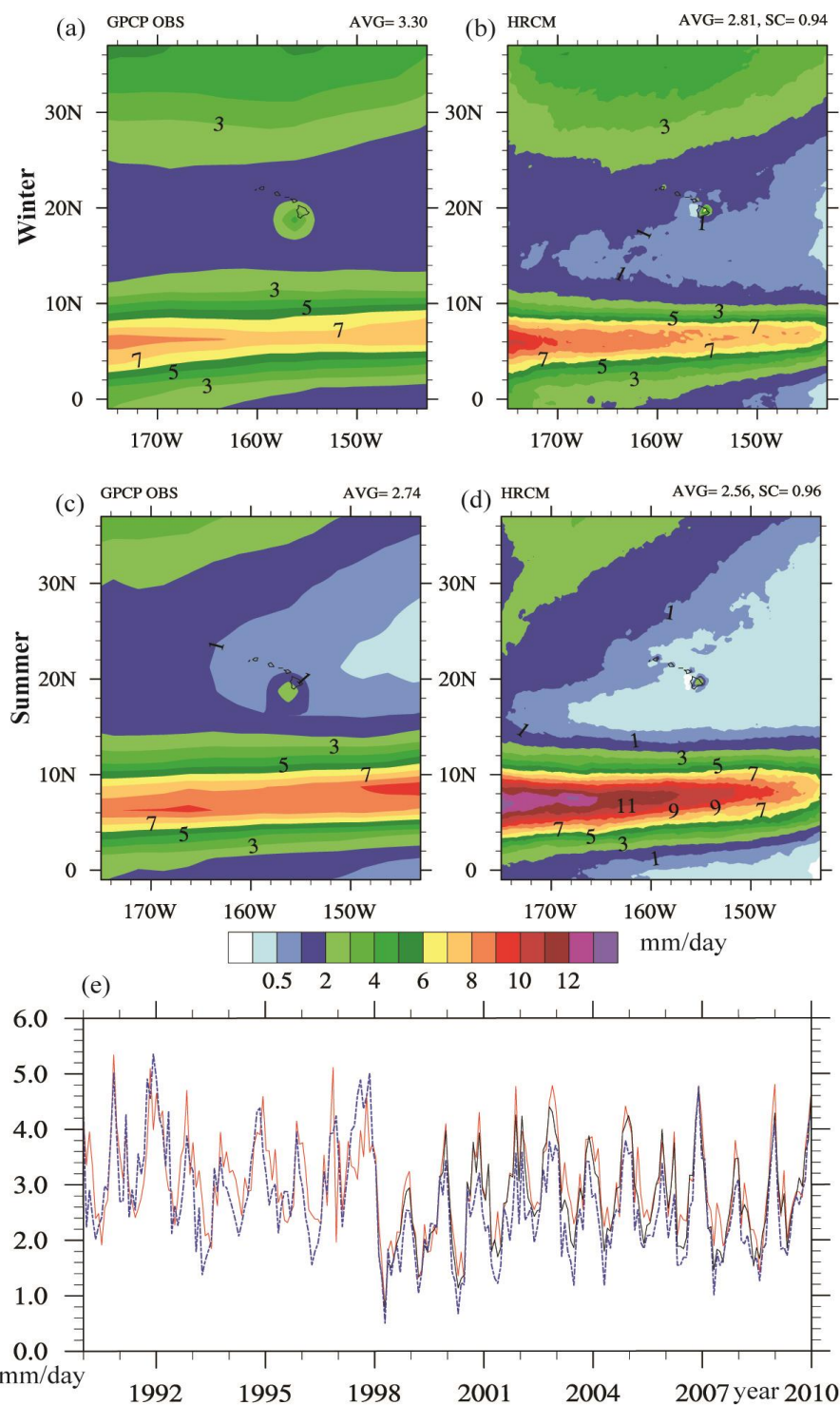
Figure 2. The 20-year mean winter precipitation in (a) the GPCP gridded observations, and (b) HRCM 15 km simulation. (c) as in (a) but for summer. (d) as in (b) but for summer. (e) The time series for the simulated monthly mean rainfall averaged over the whole domain in the model simulation (dashed blue), the GPCP observations (red) and the TRMM observations (black). SC means spatial correlation coefficient.

Figure 3. The 20-year mean geopotential height at 500 hPa (GHT500) (shaded, m) and mean sea level pressure (SLP) (contour, hPa) biases (HRCM simulation minus MERRA reanalysis data) for (a) winter, and (b) summer.

Figure 4. PDFs of the daily values over the time period 1990-2009 of (left to right): daily mean surface air temperature (SAT), daily maximum SAT, daily minimum SAT, daily mean surface specific humidity (Q_2), daily mean surface wind speed at (top to bottom) Lihue, Honolulu, Kahului and Hilo. Red lines show station observations and blue lines are for the HRCM 3 km simulation at nearest land grid points to stations. The simulated long-term mean biases (HRCM simulation minus observations) for each variable are also shown in the figure. The rightmost column is the daily rainfall histogram for each station with colored shading showing the observed values and the hatching showing the result for the HRCM 3 km simulation. The bin width for SAT is 1°C, for surface specific humidity is 1 g kg^{-1}, for wind speed is 1 m s^{-1}, and uneven for rainfall as shown by the tick marks.

Figure 5. The 20-year mean seasonal cycle for surface air temperature (SAT), wind speed and rainfall at Lihue, Honolulu, Kahului and Hilo, respectively. The red line is for station observations, and the blue line is for the HRCM 3 km simulation at the nearest land grid points. The correlation coefficient between the two curves, C, is shown at upper right corner of each panel.
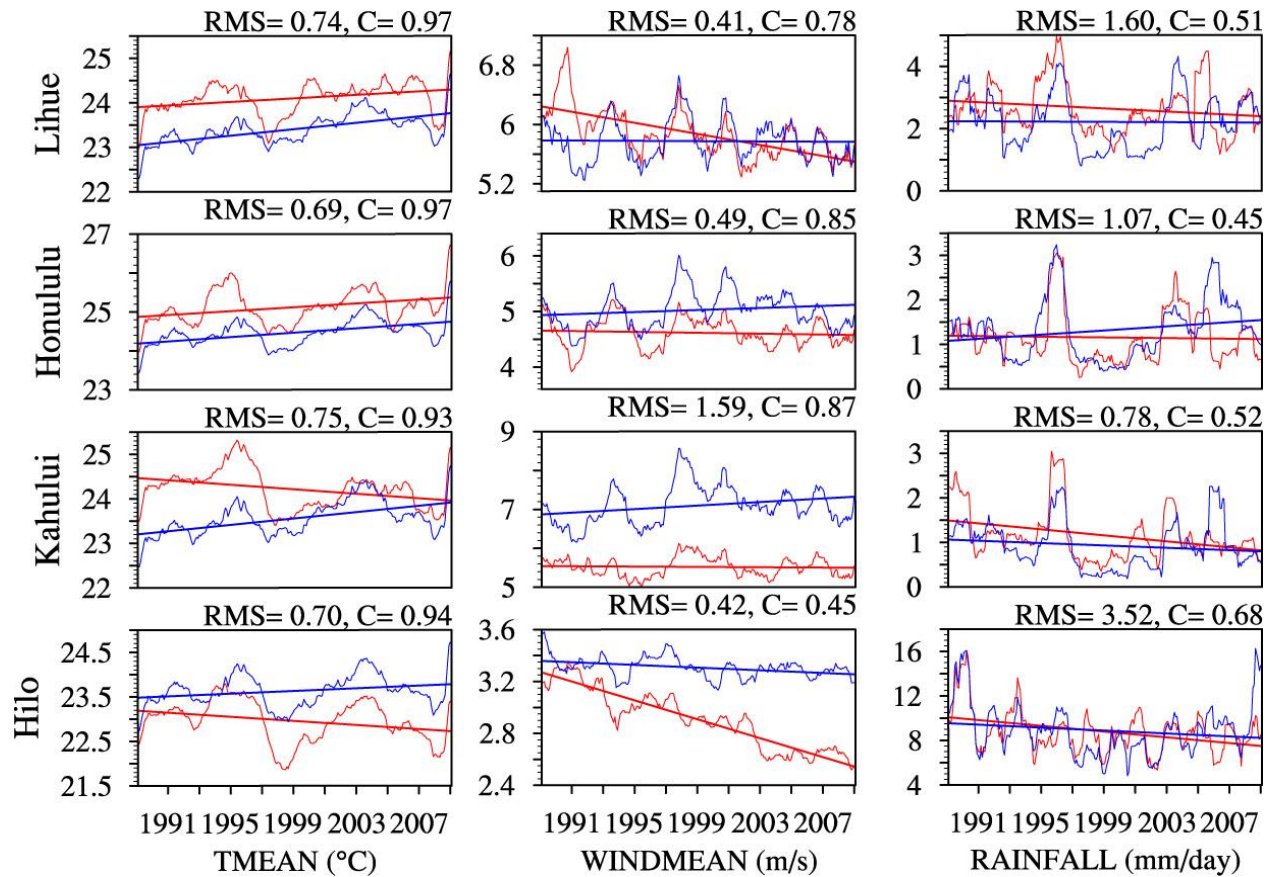
Figure 6. The time series of mean surface air temperature (SAT), wind speed and rainfall at Lihue, Honolulu, Kahului and Hilo. Quantities shown are 6-month running-means. Red curves are for the station observations, and blue is for the HRCM 3 km simulation at the land grid point nearest to the station. 'RMS' is the mean root mean square difference between model and observational curves, and 'C' is the correlation coefficient between the two curves. The least squares linear regression trends over the 20 years are also shown in each panel.

Figure 7. (a) The observed 20-year annual mean rainfall based on several hundred measurement stations (see text for details). (b) The simulated annual mean rainfall from the 3 km HRCM simulation. 'SC' is the spatial correlation over the land calculated for 3 km grids. Also shown are the averaged rainfall amounts (mm d^{-1}) over all land areas. (c) The model bias (model minus observations). The observations, model results and the model biases for winter and summer are shown in (d-f) and (g-i), respectively.
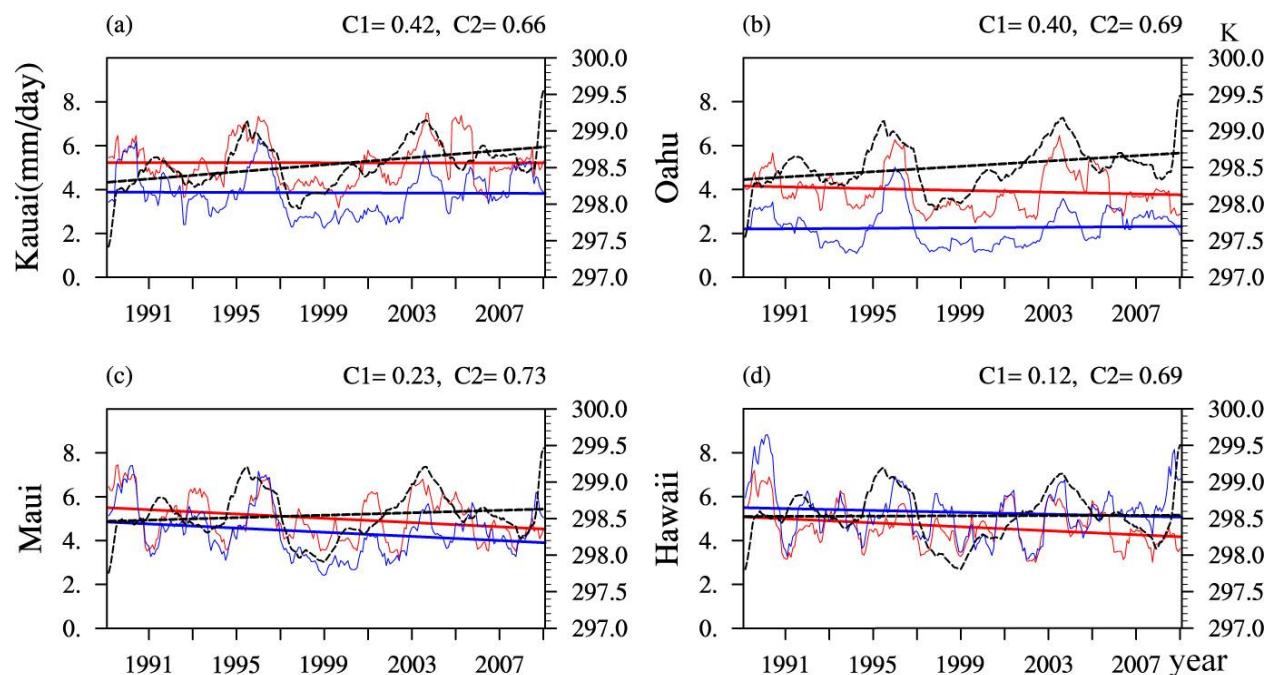
881

Figure 8. The interannual variations of the rainfall (red is for observations; blue is for the HRCM 3 km simulation) and local SST (black) for the Islands of Kauai, Oahu, Maui and Hawaii. C1 denotes the correlation coefficient between local SST and observed rainfall. C2 denotes the correlation coefficient between observed and simulated rainfall. The trends are also shown in the figure.
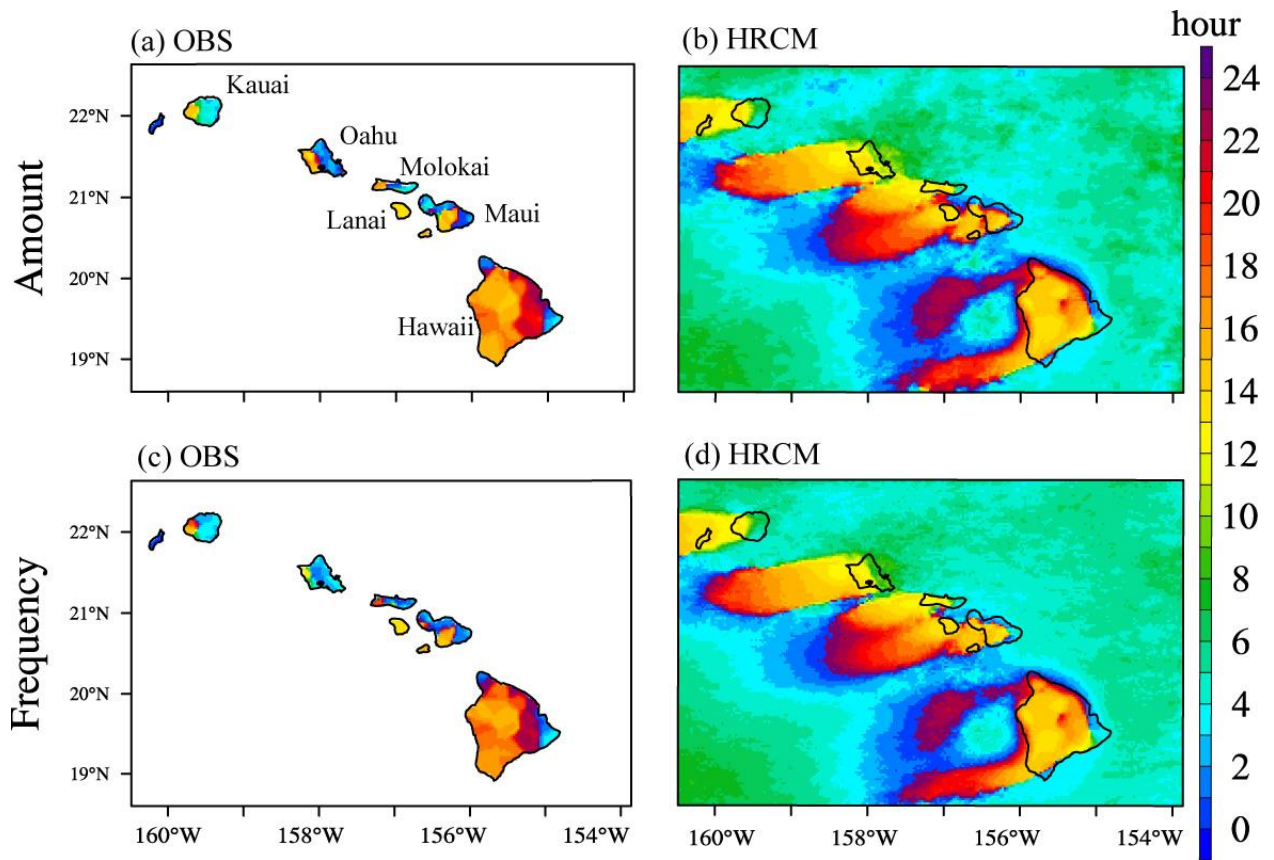
Figure 9. Phase of the diurnal harmonic of long-term mean annual-mean rainfall. Specifically shown are the local time (LT) peak of the diurnal (24-hour) harmonic of the mean rainfall rate (a, b) and rainfall frequency (c, d). Results for our gridded observations over land are in (a, c) and those for the HRCM simulation are in (b, d).
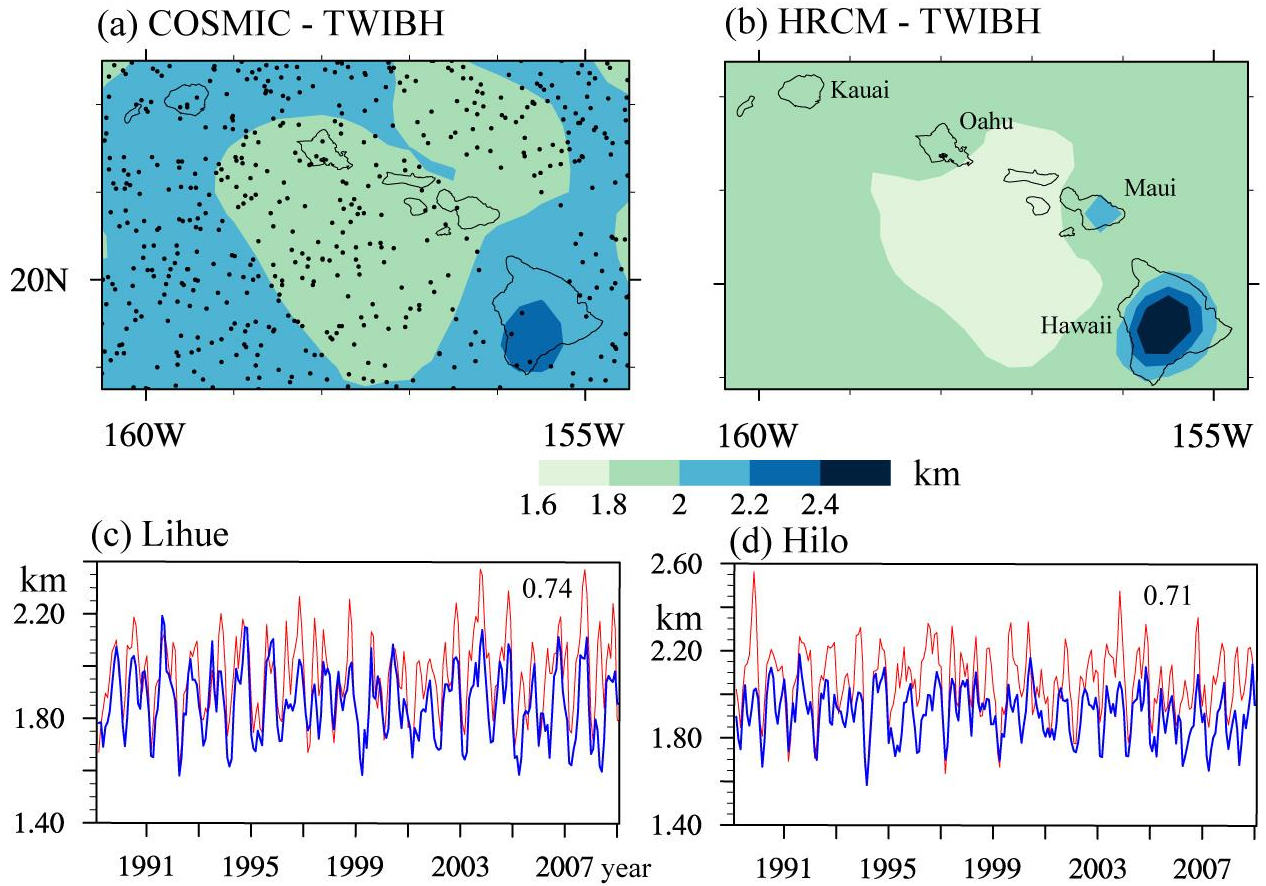
(a) COSMIC - TWIBH

(b) HRCM - TWIBH

20N

160W   155W   160W   155W

km

1.6   1.8   2   2.2   2.4

(c) Lihue

km
2.20   0.74

1.80

1.40

1991   1995   1999   2003   2007 year

(d) Hilo

2.60
km   0.71

2.20

1.80

1.40

1991   1995   1999   2003   2007

892

Figure 10. The trade wind inversion base height (TWIBH) derived from the COSMIC
observations (a) and the HRCM simulation (b). The black dots in (a) are the locations of the
observed profiles from COSMIC. The time-series of monthly mean of the TWIBH computed
from balloon soundings at Lihue and Hilo are shown by the red curves in (c) and (d),
respectively. The values from the HRCM simulation are shown by the blue curves. The
correlation coefficient between the observed and modeled time series is shown in the upper
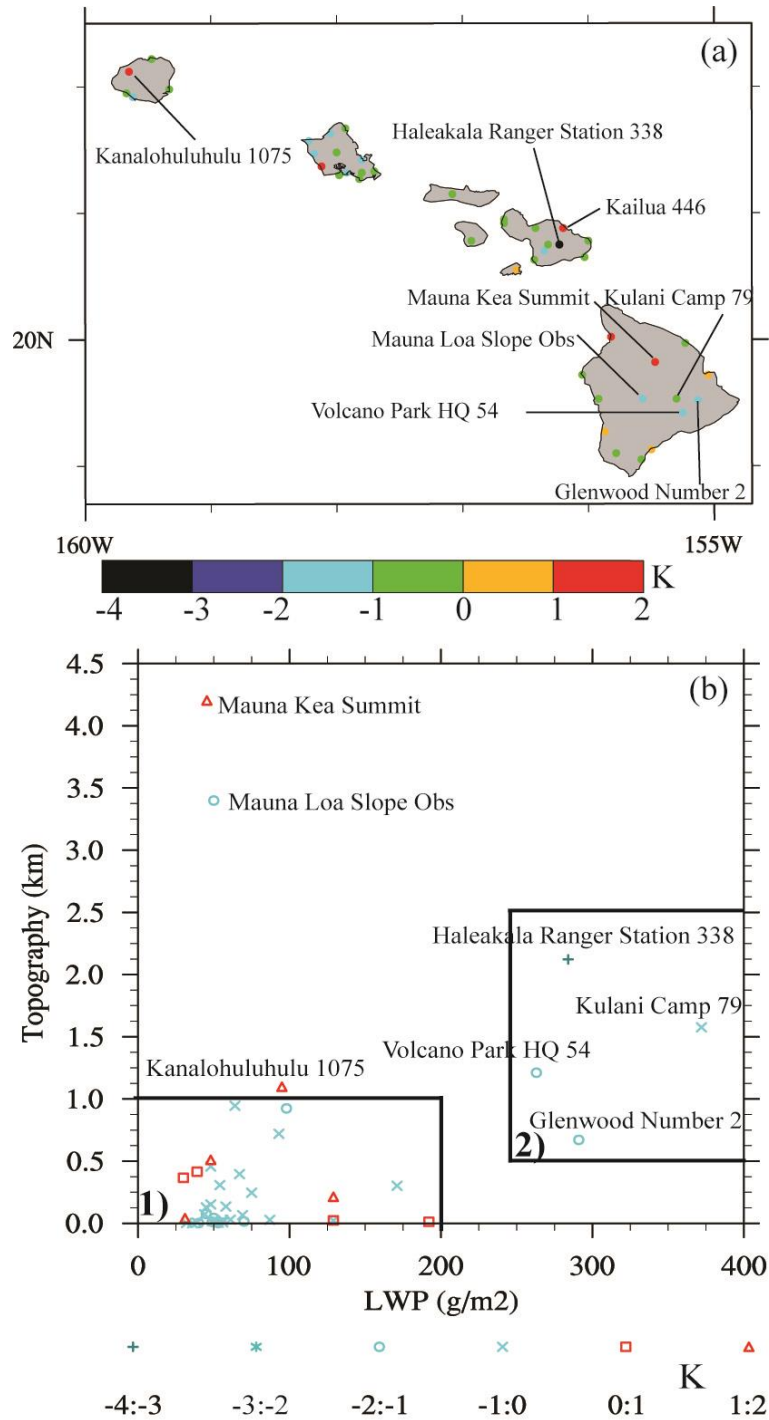right corner of each panel.

Figure 11. The distribution map for the 20-year mean surface air temperature (SAT) bias (HRCM simulations minus observations) over the Hawaiian Islands (a). The temperature biases (e.g., "1:2" means "1 to 2") for each station related to liquid water path (LWP) and topography are also shown (b). Some station names are marked in the figures. K is degrees in Kelvin. Box 1 includes the low topography stations, and Box 2 includes the stations that are in the cloud zone in the model.
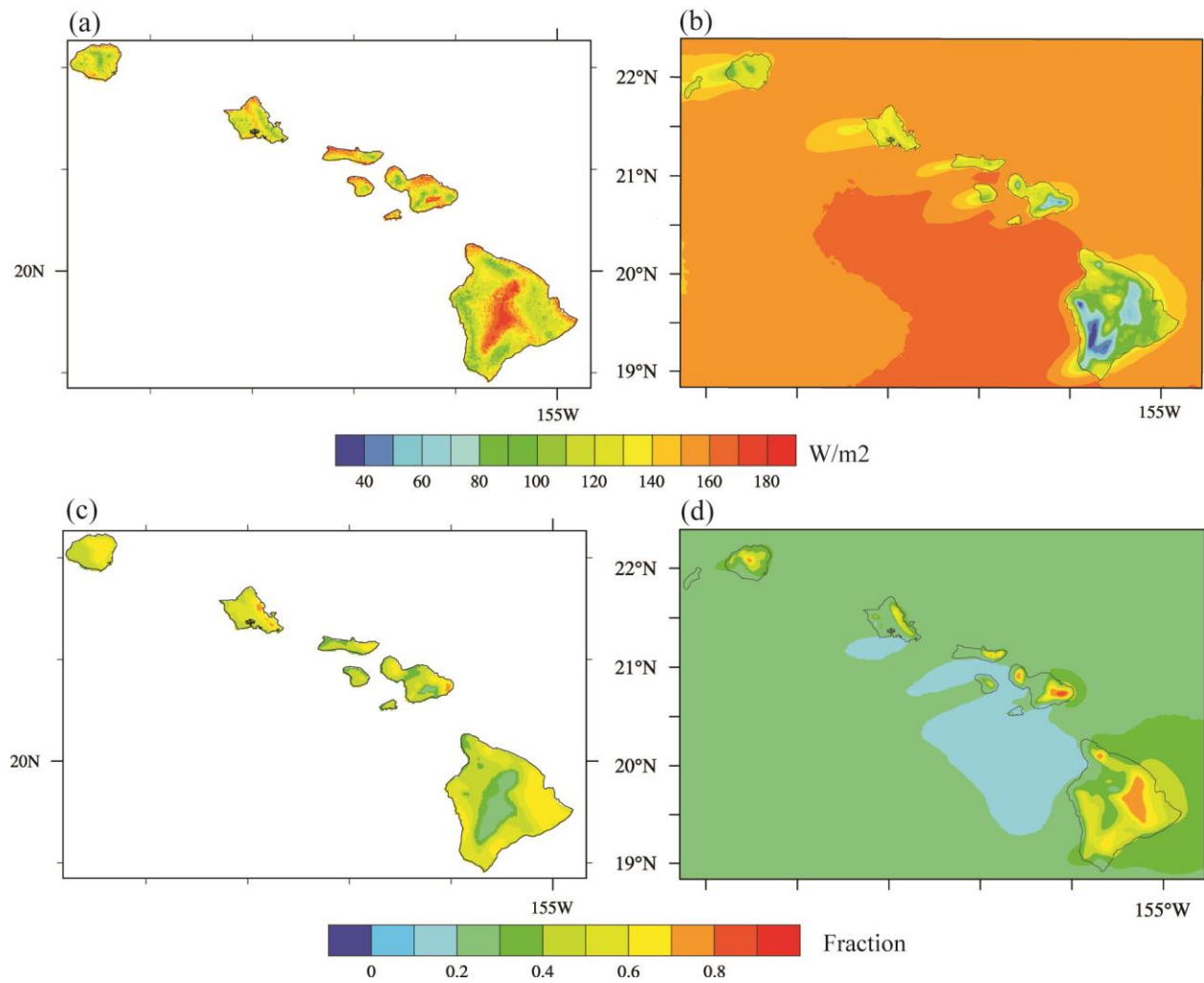
Figure 12. The retrieved net radiation at the surface (a) and total cloud fraction (c) climatology by Giambelluca et al. (2014), and the model simulated climatology of net surface radiation (b) and total cloud fraction (d).
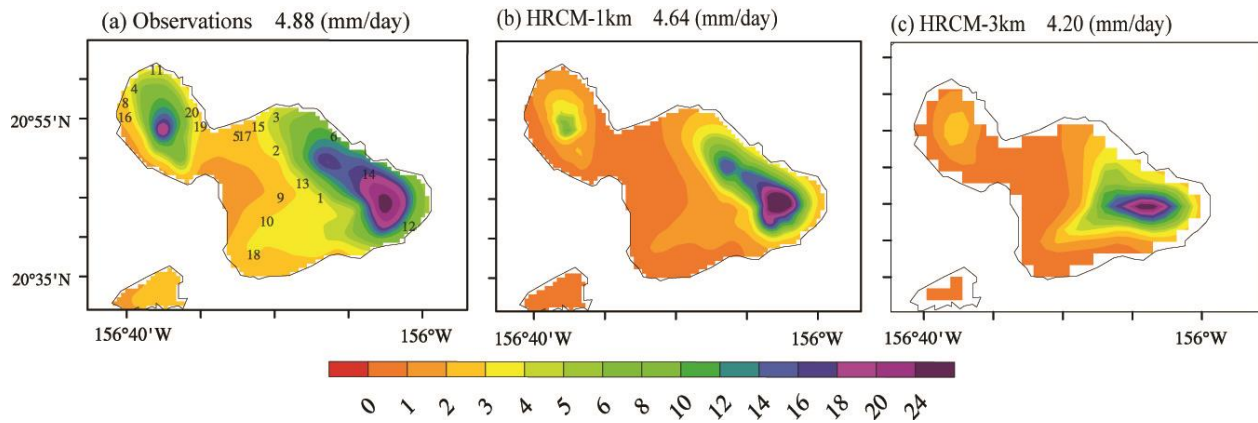
911

912 Figure 13. The 20-year mean rainfall from observations (a), the HRCM 1 km simulation (b) and
913   the HRCM 3 km simulation (c). The numbers in (a) are the NCEI observational stations
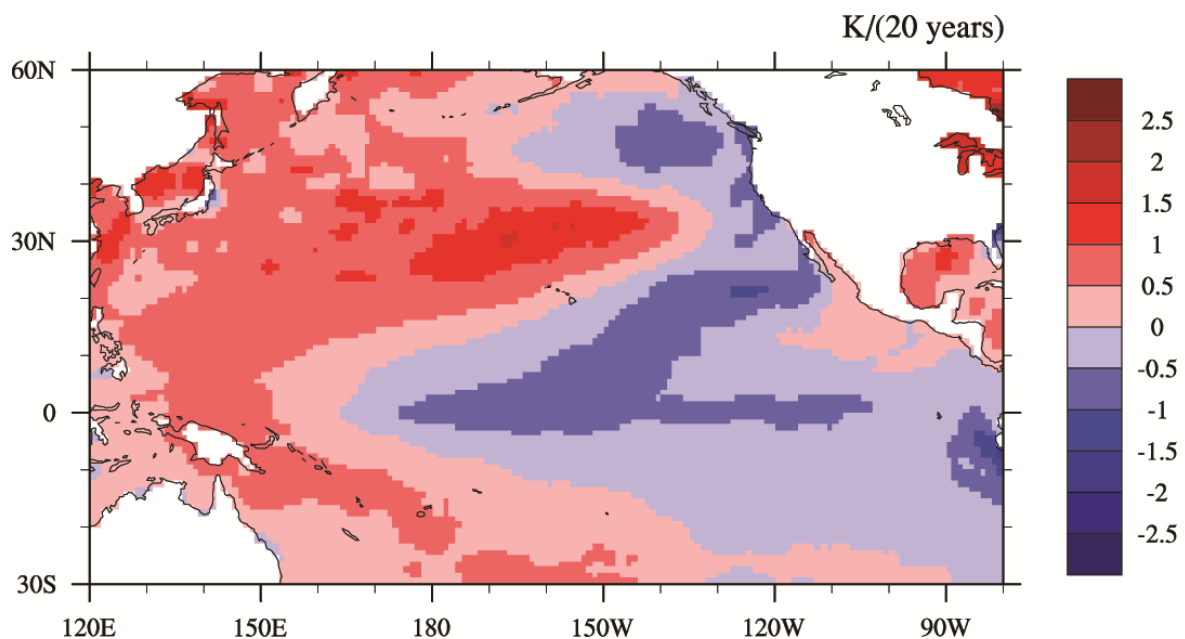914   listed in Table 2.

915

916

K/(20 years)

Figure A1. The trend in the Reynolds (2010) observed sea surface temperatures (SSTs) over the time period 1990-2009 based on a linear regression of the monthly mean values at each grid point. The trend is expressed in Kelvin (K) over 20 years.